International Journal of Heat and Mass Transfer 234 (2024) 126102

Contents lists available at ScienceDirect

International Journal of Heat and Mass Transfer

journal homepage: www.elsevier.com/locate/ijhmt

Two-phase flow instabilities during microgravity flow boiling onboard the International Space Station

Issam Mudawar [a,*], Steven J. Darges [a], V.S. Devahdhanush [a], Mohammad M. Hasan [b], Henry K. Nahra [b], R. Balasubramaniam [c], Jeffrey R. Mackey [d]

[a] Purdue University Boiling and Two-Phase Flow Laboratory (PU-BTPFL), School of Mechanical Engineering, Purdue University, 585 Purdue Mall, West Lafayette, IN 47907, USA
[b] NASA Glenn Research Center, 21000 Brookpark Road, Cleveland, OH 44135, USA
[c] Case Western Reserve University, 10900 Euclid Ave., Cleveland, OH 44106, USA
[d] HX5, LLC 3000 Aerospace Parkway, Brookpark, OH 44142, USA

ARTICLE INFO

Keywords:
flow boiling
flow instabilities
microgravity
pressure response
frequency domain analyses
International Space Station
onset of flow instabilities

ABSTRACT

This study is an elaboration on flow instabilities observed during flow boiling experiments conducted onboard the International Space Station (ISS) as part of the Flow Boiling and Condensation Experiment (FBCE). During highly subcooled flow boiling, liquid backflow into the channel that rapidly condenses vapor within the channel was observed. Experiments were conducted with an enhanced sampling frequency of 30 Hz and an extended image sequence recording duration of at least 4 seconds at 500 frames per second to further investigate the instability. Identical experiments were performed both in microgravity onboard the International Space Station (ISS) and in Earth gravity during vertical upflow. Instabilities in microgravity are more severe than those in Earth gravity and, at their most severe, propagate to the channel's upstream region. Instabilities are observed within the channel when the intensity, I, which is dependent on inlet pressure fluctuations and mass velocity, exceeds 1.8×10^5 W/m^2. Parametric trends of the frequency and amplitude of inlet pressure fluctuations during instability are examined, which reveal instabilities are most severe at low flow rates, high inlet subcoolings, and high heat fluxes. Various stability maps proposed in the literature are evaluated against the present database, and instabilities only manifest for subcooling numbers greater than 14. A subset of the database containing the Onset of Flow Instability (OFI) point is extracted to first evaluate correlations available in the literature and then develop a new correlation. The new correlation is applicable in both microgravity and Earth gravity conditions and predicts the database with a Mean Absolute Error (MAE) of 1.3%.

1. Introduction

1.1. Two-phase Systems in Aerospace Applications

Innovations in the medical, transportation, energy, aerospace, and defense industries are escalating power densities that exceed the cooling capabilities of conventional single-phase thermal management systems [1]. To meet cooling demands, thermal engineers can look to two-phase thermal management systems, which capitalize on the working fluid's latent heat to achieve significantly enhanced heat transfer coefficients. Not only are two-phase systems capable of handling greater heat loads, but they also achieve this with systems that are lighter and more compact than single-phase systems. Hence, two-phase systems have been identified as potential solutions for thermal management during future space missions [2].

Two-phase cooling can be employed in numerous configurations including capillary flows [3], pool boiling [4], falling films [5], flow boiling in macro-channels [6,7], flow boiling in mini/micro-channels [8], jet impingement [9], sprays [10], and hybrid cooling schemes [11,12]. Macro-channel and mini/micro-channel flow boiling rely on fluid motion (rather than body force) to flush bubbles away from heated surfaces and replenish it with fresh liquid. It is capable of handling high heat fluxes while meeting minimal size constraints (often using *cold plates*). Channel flow boiling is well suited to cooling high-heat-flux surfaces in space applications and will be the primary focus for the

* Correspondence; Tel. (765) 494-5705; Fax (765) 494-0539; website:
E-mail address: mudawar@ecn.purdue.edu (I. Mudawar).
URL: https://engineering.purdue.edu/BTPFL (I. Mudawar).

https://doi.org/10.1016/j.ijheatmasstransfer.2024.126102
Received 11 May 2024; Received in revised form 18 July 2024; Accepted 19 August 2024
Available online 24 August 2024

Nomenclature

A_c	channel cross-sectional area, [m^2]
Bd	Bond number, $g(\rho_f - \rho_g)D^2/\sigma$
Co	Confinement number, $\sqrt{g(\rho_f - \rho_g)D^2/\sigma}$
c_p	specific heat, [J/kg.K]
D	diameter; hydraulic diameter, [m]
Dp	pressure drop, [Pa]
f	frequency, [Hz]
G	mass velocity, [kg/m^{2}s]
g	gravitational acceleration, [m/s^2]
g_e	gravitational acceleration on Earth, [m/s^2]
μg_e	microgravity, [m/s^2]
H	height of channel, [m]
h	enthalpy, [J/kg]
h_{fg}	latent heat of vaporization, [J/kg]
I	pressure fluctuation intensity, $I = \Delta p^2/2G$, [W/m^2]
Ja^{**}	modified Jacob number
L	length, [m]
L_{cap}	capillary length, $L_{cap} = \sqrt{\sigma/g(\rho_f - \rho_g)}$, [m]
$\dot{m}$	mass flow rate [kg/s]
N	number of data points
N_{pch}	phase change number, $N_{pch} = \frac{q''_w P_h L_h}{GA_c h_{fg}} \times \frac{(\rho_f - \rho_g)}{\rho_g}$
N_{sub}	subcooling number, $N_{sub} = \frac{(h_f - h_{in})}{h_{fg}} \times \frac{(\rho_f - \rho_g)}{\rho_g}$
P	perimeter, [m]
p	pressure, [Pa]
q''_w	heat flux, [W/m^2]
q''_{CHF}	critical heat flux, [W/m^2]
Re_{fo}	Reynolds number, GD/μ_f
T	temperature, [°C]
ΔT_{sub}	fluid subcooling, $T_{sat} - T_f$, [°C]
t	time, [s]
W	width of channel, [m]
We_{fo}	Weber number, $G^2D/(\rho_f\sigma)$
x_e	thermodynamic equilibrium quality, $x_e = \frac{h - h_f\|_p}{h_{fg}\|_p}$
z_i	coordinate direction, $i = 1$, 2, or 3

Greek symbols

μ	dynamic viscosity, [kg/m-s]
ξ_{10}	percentage of datapoints predicted within ±10%
ρ	density, [kg/m^3]
σ	surface tension, [N/m]
φ	measured signal

Subscripts

d	development
e	exit
exp	experimental
f	saturated liquid; fluid
g	saturated vapor
h	heated
in	inlet
out	outlet
$peak$	peak frequency
$pred$	predicted
sat	saturation
sub	subcooling
w	wetted
wa	heated wall (= $w1$ or $w2$)

Acronyms

BHM	Bulk Heater Module
CHF	Critical Heat Flux
DWO	Density Wave Oscillation
FBCE	Flow Boiling and Condensation Experiment
FBM	Flow Boiling Module
ISS	International Space Station
MAE	Mean Absolute Error (%)
nPFH	n-Perfluorohexane
OFI	Onset of Flow Instability
ONB	Onset of Nucleate Boiling
PDO	Pressure Drop Oscillation
RTD	Resistance Temperature Detector
UTC	Coordinated Universal Time

present study.

1.2. Flow Boiling in Microgravity

The vast majority of design tools are developed and validated with data acquired in Earth gravity. However, the heat transfer performance, pressure drop, and flow patterns during flow boiling in microgravity (μg_e) are expected to deviate from those in Earth gravity, exacerbating the uncertainty when applying various correlations or models. To broaden the applicability of flow boiling design tools to μg_e environments, researchers have utilized drop towers (*e.g.*, Ma and Chung [13] and Liu et al. [14]) and parabolic flights (*e.g.*, Narcy *et al.* [15], Lebon *et al.* [16], and Iceri *et al.* [17]) to obtain data in reduced gravity. Generally, both bubble size and vapor production increase during the temporary periods of μg_e compared to g_e, resulting in degraded heat transfer and CHF values in μg_e. However, at elevated flow rates, flow inertia mitigates the impact of gravity.

While the insights from short duration μg_e experiments are invaluable, each experimental method has inherent shortcomings. Experiments performed in drop towers may not reach steady state and long-duration transients will not be captured in their short periods of μg_e [18]. Parabolic flights are prone to *g-jitter* [19], which degrades the level of μg_e and may artificially enhance heat transfer. Therefore, flow boiling data acquired in steady μg_e, such as on the International Space Station (ISS) [20], are required to develop and validate reliable design tools.

A few research groups have been afforded the opportunity to investigate flow boiling on the ISS. Researchers in conjunction with JAXA investigated two-phase flow patterns and heat transfer during flow boiling of n-Perfluorohexane (nPFH) in a copper and glass heated tube in μg_e. Their experiments were performed onboard the ISS as part of the *Two-Phase Flow Experiment* between 2017 and 2019. Thus far, detailed heat loss results have been reported for subcooled [21] and two-phase inlet [22].

The *Flow Boiling and Condensation Experiment* (FBCE) is a long-term collaborative project between the Purdue University Boiling and Two-Phase Flow Laboratory and NASA Glenn Research Center. The goal of FBCE is to obtain both flow boiling and condensation data in μg_e, via the ISS. Prior to launching the experimental rig to the ISS, it was used to perform flow boiling experiments in Earth gravity with both subcooled [23] and saturated inlet [24]. The first stage of FBCE collected flow boiling data onboard the ISS during February 2022 – July 2022. Valuable experimental results and assessment of various parametric trends have been reported for heat transfer with subcooled inlet [25,26] and saturated inlet [27], and critical heat flux (CHF) with subcooled [28] and saturated [29] inlet conditions in μg_e. Consolidated databases were utilized to assess the applicability of various seminal correlations, to

propose new correlations for both heat transfer coefficient [30] and critical heat flux (CHF) [31] and to develop a methodology for the development of Artificial-Neural-Network-based prediction tools for μg_e flow boiling [32].

1.3. Flow Boiling Instabilities

1.3.1. Classifications of Instability

Instabilities are undesirable in two-phase flow loops and have been the subject of extensive research. In fact, numerous literature reviews have been published over the years [33–37], compiling the findings of various researchers. This has resulted in several general classifications for two-phase instabilities, while the mechanisms and effects of each are more nuanced.

Two-phase instabilities can be broadly categorized as either *static* or *dynamic*. *Static instabilities* consist of a one-time excursion from one set operating conditions to another. *Static instabilities* include CHF, Ledinegg instability, boiling curve hysteresis, vapor burst, and flow pattern transition instability. CHF occurs when vapor production prevents liquid contact with the heated wall, and the mechanism of heat transfer transitions from nucleate boiling to film boiling. This is accompanied by an unsteady rise in surface temperatures, which could potentially lead to surface dryout and device failure.

Extensive information is available regarding the mechanism and prevention of Ledinegg instability [34], which occurs when the slope of the pressure-drop-versus-mass-velocity curve of the pump (*external characteristic curve*) is greater than that of the flow loop, predominantly the test section, (*internal characteristic curve*). Physically explained, the pressure head supplied by the pump in response to a perturbation in flow rate causes the system to be driven further away from its original operating point. This can occur during flow boiling when increasing flow rate decreases pressure drop, resulting in an internal characteristic curve with a negative slope. Fig. 1 depicts an internal characteristic curve for a channel exposed to constant heat flux and examples of three different external characteristic curves.

At point A, flow boiling occurs, and the fluid is in a saturated two-phase state. Increasing flow rate results in decreased vapor production and system pressure drop. This is contrary to the single-phase region where increasing flow rate monotonically increases pressure drop. The external characteristic curve of a positive displacement pump, which operates at fixed flow rates, is represented by case 1. The near-infinite negative slope of the external characteristic curve prevents Ledinegg instability. Case 2 represents coupled pressure drop and mass velocity due to the fixed-speed operation of centrifugal pumps. The example depicted by case 2 has a less negative slope than the internal curve and would be susceptible to Ledinegg instability. A perturbation of flow rate within the system invokes a greater change in system pressure drop than the variation in pump pressure head at the new flow rate. This drives the flow rate further away from point A until a new stable operating condition is reached, where system pressure drop equals pump pressure head, and the internal characteristic curve is less negative than the external characteristic curve. This results in a new stable operating condition with a flow rate either greater than (point B_2) or lesser than (point C_2) the original operating condition (point A). Similarly, constant pressure drop systems, depicted by case 3, are prone to Ledinegg instability due to their zero-slope characteristic curve, and a perturbation in flow rate at point A would cause an excursion to points B_3 or C_3. Ledinegg instability causing an excursion to a low flow rate, such as points C_2 or C_3 in Fig. 1, can be dangerous and trigger CHF. However, Ledinegg instability can be prevented by avoiding the negative slope

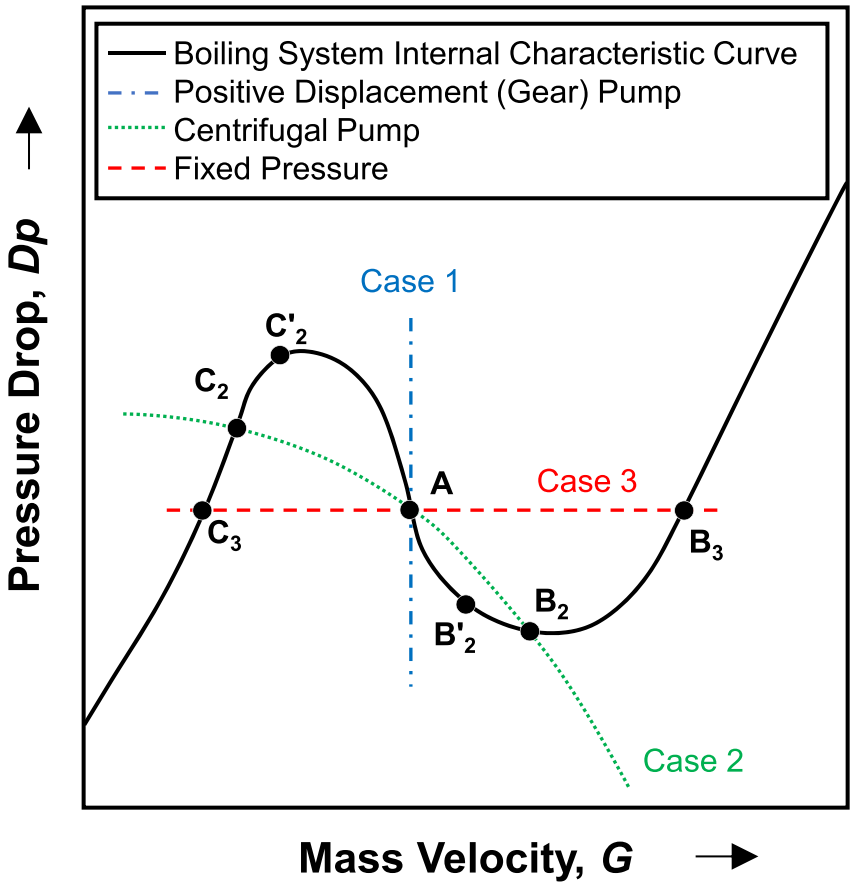

Fig. 1. Pressure drop versus mass velocity characteristic curves during describing a system's inclination for instability during flow boiling with a (1) positive displacement pump, (2) centrifugal pump, and (3) fixed pressure drop boundary condition.

region of the characteristic curve, typically given as operating constraints [38–40]. Alternatively, the system can be modified to eliminate the negative slope of the internal characteristic curve. This is commonly accomplished by throttling the flow upstream, increasing frictional pressure drop and reducing the significance of the two-phase component of total pressure drop [41].

Boiling curve hysteresis creates deviations in the boiling curve near the onset of nucleate boiling (ONB) when increasing or decreasing the heat flux. It is prevalent for fluid and surface combinations with low contact angle and is attributed to the difference in wall superheat required to initiate and halt nucleate boiling [42]. Vapor burst can be a consequence of boiling curve hysteresis with a well degassed fluid. It occurs when liquid temperature exceeds the local saturation temperature and ONB triggers severe flashing of liquid to vapor [43]. As the name implies, flow pattern transition instability occurs when a minor perturbation in operating conditions causes a transition to a new flow regime with distinct pressure drop and heat transfer characteristics.

Flow pattern transition instability can also appear as a *dynamic instability*, with alternating flow patterns [44]. *Dynamic instabilities* continuously cycle between marginally unstable operating conditions, unlike the singular excursion which characterizes *static instabilities*. Other common dynamic instabilities include density wave oscillations (DWOs), parallel channel instability (PCI), and pressure drop oscillations (PDOs).

A review by O'Neill and Mudawar [35] provided a detailed mechanistic description of DWOs. In summary, DWOs result in the location of the boiling boundary to oscillate within the channel. This is caused by the pressure drop in single-phase and two-phase length of channel responding out of phase to one another in response to a perturbation in flow rate, due to the different propagation speeds in the two regions. DWOs could be triggered by several factors. Fukuda and Kobori [45] identified 5 distinct variations of DWOs in their system which differed by root cause. They analytically demonstrated DWOs were attributed to either acceleration in the heated section, friction in the heated section, friction in the riser section, gravity in the heated section and inertia of single-phase fluid, or gravity in the riser section.

In some cases, DWOs result in unusual flow dynamics. For instance, Khodabandeh and Furberg [46] observed thermal oscillations during flow boiling of R-134a in a natural circulation loop with a vertically oriented evaporator. This was attributed to flow stagnation and reversal disrupting nucleate boiling in the channel. O'Neill *et al.* [47] observed DWOs during flow boiling experiments of FC-72 in a vertical rectangular channel. DWOs manifested as the alternating passage of liquid dominant, *high-density fronts*, and vapor dominant, *low-density fronts*, through the channel during saturated flow boiling. The DWOs were a consequence of buoyancy-induced phase separation, leading to an accumulation of liquid at the inlet and vapor at the outlet of channel. This, in turn, increased the inlet pressure until a liquid wave, or high-density front, was forced through the channel. They showed that the dominant frequency of inlet pressure fluctuations was correlated to the passing of high- and low-density fronts.

In parallel channels, the feedback of instabilities in individual channels to one another through shared plenums increases the complexity of each aforementioned instability. In some cases, the mechanism of instability in individual channels is identical to those already described, but the presence of multiple flow paths can cause the system to react differently. For example, in the presence of DWOs, the flow rate in individual channels can oscillate either out of phase with one another, while the total flow rate is constant, or in phase with one another, while the total flow rate oscillates [48].

Similar to Ledinegg instability, PDOs occur while operating in the negative slop region of the internal characteristic curve. PDOs are caused by interactions between the pump, heated section, and the compressible volume, and are considered a system-level instability, as opposed to device-level instabilities like DWOs and PCI. In fact, PDOs can be thought to occur as the system attempting to undergo Ledinegg instability, but the inertia of liquid flowing into or out of the accumulator or reservoir in response to the adjustment of pressure drop and flow rate prevents the system from reaching a new steady condition [34]. This results in the system oscillating between two marginally stable conditions, depicted in Fig. 1 as points B'$_2$ and C'$_2$. The lagged response of the compressible volume results in out-of-phase oscillations of pressure drop and flow rate, typically with larger amplitude and longer periods than DWOs or PCI. However, the inclusion of a compressible volume does not completely eliminate the possibility of excursive instabilities, and some systems are prone to both Ledinegg and PDOs [49].

1.3.2. Influence of Gravity on Flow Instabilities

Gravity significantly influences two key areas of flow boiling relevant to instabilities – bulk fluid motion and bubble growth. Body force is present in the conservation of momentum of fluids, and in some cases, acts as the dominant term driving fluid motion, *i.e.*, falling films. Consequently, gravity influences pressure gradient, void fraction, phase velocities, and flow regime, which specifically affects frictional pressure drop. As discussed in the context of Ledinegg instability and PDOs in the previous subsection, a system's inclination for instabilities is determined by how pressure drop responds when flow rate is perturbed.

One of the first experiments identifying instabilities in μg_e flow boiling was performed by Papell [50], who studied flow boiling of water in a circular channel onboard a parabolic flight. An instability emerged in μg_e which was not observed in terrestrial experiments. A momentary interruption of flow caused a transition from highly subcooled bubbly flow to slug flow, augmenting heat transfer coefficient by 16%.

The short periods of μg_e achieved by parabolic flights and drop towers hinder the investigation of instabilities during steady operation. Schlichting [51] numerically studied the effects of gravity on flow boiling stability using the homogenous flow and drift flux models via both linear and non-linear methods. The author incorporated accumulator dynamics into a transient flow model and predicted flow rate oscillations in the test section, typical of DWOs or PDOs. In a steady state model, a negative slope on the characteristic curve was predicted for a broader range of flow rates in μg_e than g_e, suggesting the loop would be more susceptible to PDOs in μg_e. However, due to a lack of μg_e data, the models were validated only for Earth gravity.

Gravity is also crucial during bubble growth. Capillary length, traditionally used as the characteristic length scale of a bubble, is defined as

$$L_{cap} = \sqrt{\frac{\sigma}{g(\rho_f - \rho_g)}}. \tag{1}$$

The definition suggests that larger bubbles tend to form in reduced gravity. In fact, L_{cap} diverges to infinity in μg_e as the gravitational acceleration (g) approaches zero. Confinement number is defined based on capillary length as

$$Co = \frac{L_{cap}}{D}, \tag{2}$$

and is commonly used as transition criteria from macro- to micro-channels. Although a range of Co values have been proposed as transition criteria, typically around unity, a channel is generally considered a micro-channel if the diameter approaches the capillary length of bubbles. Reliance on a strict cut-off value based on Co could potentially misrepresent the flow boiling physics in microgravity where $Co >> 1$, irrespective of the channel size. In macro-channels, bubbles are small compared to the channel's diameter, the channel's cross-sectional area insignificantly influences bubble growth, and the structure of vapor is based on the coalescence of individual bubbles. He *et al.* [52] provided a simple description for the three stages of bubble growth in micro-channels: (i) *free growth* immediately begins after nucleation, with bubbles growing spherically, unconstrained by the channels, (ii) *partially confined growth* begins once a bubble grows large enough to

touch another wall, and further expands into the channel's cross-section, and lastly (iii) *fully confined growth* begins once the bubble occupies the channel's entire cross-section and is forced to expand axially. The unique bubble behavior in macro- and micro-channels potentially causes distinct instability mechanisms. For instance, DWOs in micro-channels are strongly linked with flow reversal, caused by axial bubble expansion towards the inlet, during fully confined bubble growth.

Flow boiling of FC-72 in a 2, 4, and 6 mm diameter tube was examined in parabolic-flight μg_e by Baltis *et al.* [53]. They found that decreasing the diameter reduced the range where gravity influenced heat transfer, but the smallest tube diameter was prone to instabilities and premature CHF in μg_e. After the μg_e period concluded and gravity increased, stable flow boiling resumed, indicating that flow boiling in μg_e may be more prone to instabilities in certain cases. This was most likely caused by a transition from macro-channel behavior to that of a

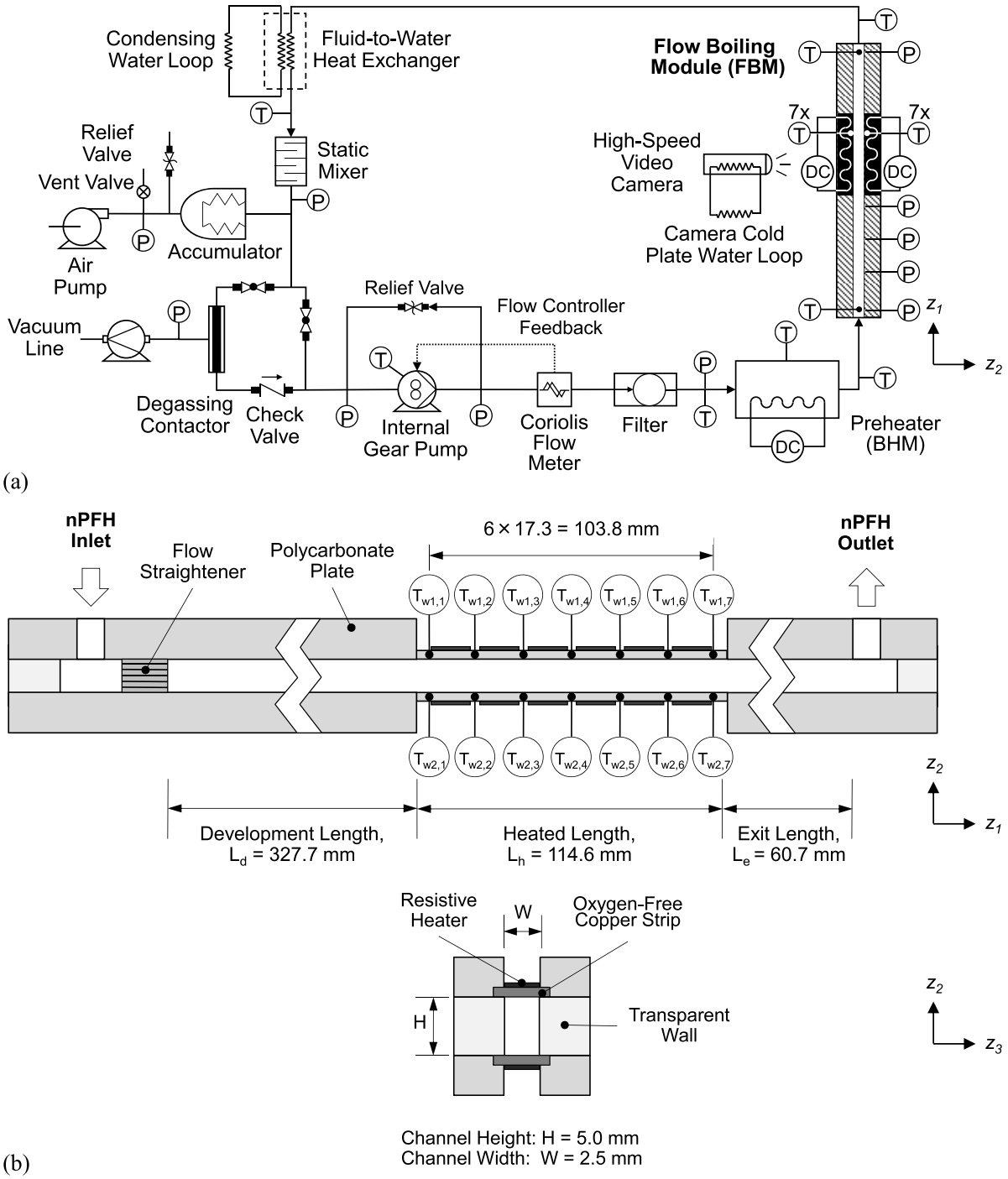

Fig. 2. Schematic diagrams of (a) the two-phase flow loop and (b) the FBM including designation of wall temperature measurements and key dimensions (adapted from [29]). The axes to the right side of each schematic show its orientation.

mini- or micro-channel.

1.4. Objectives of Present Study

Instabilities were previously reported during microgravity flow boiling experiments conducted onboard the ISS as part of FBCE [25,26,28], and manifested during high inlet subcooling as liquid backflow into the channel. While the FBCE system onboard the ISS is not optimized to study instabilities, software modifications enabled experiments to be conducted with an enhanced data sampling rate of 30 Hz and image recording duration of at least 4 seconds at 500 frames per second. The present study presents the results of experiments conducted in both μg_e onboard the ISS and in Earth gravity in vertical upflow. Abnormal flow behavior in the channel is investigated and correlated to oscillations in inlet pressure. A criterion to identify instability within the channel is established, and parametric trends of the frequency and amplitude of inlet pressure fluctuations are examined. The database is used to evaluate instability maps and correlations available in the literature and then develop a new correlation for the outlet quality corresponding to Onset of Flow Instability (OFI) in both μg_e and g_e.

2. Experimental Methods

Comprehensive details regarding the flow loop, its implementation on the ISS, test module construction, instrumentation, measurement uncertainties, operating procedure, and data reduction are provided in [25]. The present section is summarized to only include information imperative to the present study.

2.1. Two-Phase Flow Loop

Schematics of the two-phase flow loop installed onboard the ISS for flow boiling experiments are illustrated in Fig. 2 (a). The gear pump positively displaces liquid n-Perfluorohexane (nPFH), which is used due to its potential in aerospace applications [54]. A Coriolis flow meter, immediately downstream of the pump, measures the flow rate and provides feedback to the pump to maintain the desired flow rate. The fluid then passes through a filter prior to entering the preheater, named the Bulk Heater Module (BHM). The BHM heats the fluid to the desired test section inlet temperature. The fluid then enters the Flow Boiling Module (FBM), where boiling occurs, detailed measurements are taken, and images of flow patterns are captured. The fluid inlet temperature, T_{in}, outlet temperature, T_{out}, inlet pressure, p_{in}, and the outlet pressure, p_{out}, are measured by type-E thermocouples inserted directly into the flow and absolute-pressure-transducers immediately upstream and downstream of the FBM's heated length. The two-phase mixture exits the FBM, rejects heat in a fluid-to-water heat exchanger, passes through a static mixer to ensure thermodynamic uniformity, and returns to the pump as a subcooled liquid. An accumulator consisting of stainless-steel bellows, which separate the nPFH and air, is connected at a T-junction between the static mixer and the pump. The accumulator's air-side pressure is controlled by an air pump and vent valve and helps set the system pressure. Pressures across the flow loop are measured by absolute pressure transducers, and temperatures by type-E thermocouples and RTDs. The maximum measurement uncertainty in temperature is $\pm 0.5^{\circ}$C, pressure is ± 0.7 kPa, FBM heater power is $\pm 0.3\%$ of reading, BHM heater power is $\pm 0.6\%$ of reading, and mass flow rate is $\pm 0.6\%$ of reading. The response time of the pressure transducers and the flow meter, which are relied upon for high frequency measurements, are less than 1 ms and 200 ms, respectively.

The fluid was routinely degassed to remove non-condensable gases and obtain reliable data. Two alternate paths exist between the accumulator T-junction and the pump. One path is used exclusively during degassing and routes the fluid through the degassing contactor. The other is used during routine operation to bypass the degassing contactor and provide direct access to the pump.

In addition to those performed on the ISS, experiments were conducted with a ground rig located at NASA Glenn Research Center. The primary components of the ground flow loop replicate those of the flight unit, and the FBM was oriented for vertical upflow.

2.2. Flow Boiling Module

The FBM, depicted in Fig. 2 (b), is constructed by clamping together three transparent polycarbonate plates between two aluminum support plates. The flow channel is formed by milling 5.0 mm high and 2.5 mm wide slot into the middle polycarbonate plate. The FBM's flow channel consists of a 327.7 mm developing length containing a honeycomb flow straightener, a 114.6 mm heated length, and a 60.7 mm exit length. The heated walls are formed by 114.6 mm long, 15.5 mm wide, and 1.04 mm thick oxygen-free copper strips embedded into the top and bottom polycarbonate blocks. Each copper strip has six thick-film, 188-Ω, resistive heaters, electrically connected in parallel, soldered to the backside, opposite the flow channel. The temperature of the heated walls is measured by thermocouples inserted into the copper strips between each successive resistive heater. The design of the heated walls ensures uniform heat flux and fast temperature response [55].

Visual observation of flow physics within the FBM's heated length is possible through the transparent polycarbonate insulative walls. The middle polycarbonate plate containing the rectangular flow channel was vapor polished to provide distortion-free viewing surfaces. The upper and lower polycarbonate parts were also vapor polished to minimize vignetting effects that would have otherwise occurred if the plates were partially opaque or had poor surface quality. The only remaining vignetting effects caused by the embedded copper strips and O-rings were necessary for the construction of the FBM test section. After vapor polishing, all polycarbonate plates were annealed to relieve mechanical stresses induced by machining and vapor polishing. A high-speed video camera is directed at one of the transparent polycarbonate walls, and the opposite wall is backlit with blue light emitting diodes (LEDs) through a light-shaping diffuser and secondary Teflon diffuser to improve uniformity due to volume constraints. The camera is fitted with a F#0.95-25 mm lens and captures images of the heated length with spatial resolution of 100 μm imaged over 2040 × 164 pixel elements of the camera sensor arrays. Images are recorded of the final 28 seconds of each heating increment at 500 frames per second to capture any low frequency phenomena. However, after observing the period of flow transients being less than 1 second, the recorded duration was reduced to 4 seconds for some cases. Each image is saved with its corresponding time stamp in UTC for comparison to transient data. Images presented in this paper have undergone post-processing to enhance the visibility of flow features without introducing any artificialities.

2.3. Operating Procedure and Data Processing

Each test case is initiated by remotely setting the desired inlet conditions (flow rate, pressure, and quality). Once steady state is detected, DC power is supplied to the FBM heaters. Power can be supplied to either one or both sets of FBM heaters to study either single- or double-sided heating, respectively. The present study exclusively examines single-sided heating since instabilities in this heating configuration were more severe. Data is recorded for 180 seconds at 30 Hz at each heating increment, followed by a step increase in FBM heater power. Each sample of data is recorded with its corresponding time in UTC to enable comparison to the recorded images. The final 120 seconds of data at each heating increment are used to obtain steady operating conditions and analyze the frequency spectrum of transient signals. Twelve heater set points are preselected based on an estimated q''_{CHF} to span the boiling curve but avoid CHF. The experiments are terminated prior to the conclusion of the twelfth increment if one of the FBM heated-strip temperatures reaches 122°C, which is used as an indicator of CHF for safety concerns and triggers a heater shutdown.

The enthalpy of the subcooled liquid entering the FBM is determined by

$$h_{in} = h|_{T_{in}, p_{in}}. \tag{3}$$

Thermophysical properties of nPFH are evaluated using NIST-REFPROP [56]. The fluid enthalpy at the FBM's outlet is determined via energy balance as

$$h_{out} = h_{in} + \frac{q''_w P_h L_h}{\dot{m}}, \tag{4}$$

where q''_w is wall heat flux, $\dot{m}$ mass flow rate, and L_h heated length. P_h corresponds to the heated perimeter of the channel, which in the present study is equal to channel width, W. q''_w is calculated as the FBM heater power divided by the heated area, due to FBM heat loss being negligible compared to supplied power [25]. Thermodynamic equilibrium quality is determined as

$$x_e = \frac{h - h_f|_p}{h_{fg}|_p}, \tag{5}$$

where the inlet and outlet values are determined by setting $h = h_{in}$ and h_{out}, respectively, and p is the local pressure. A summary of the collected database's parametric ranges is provided in Table 1.

3. Observation of Instability

3.1. Evolution of Instability upon Increasing Heat Flux

This subsection analyzes the flow visualization and transient pressure signals during a single experimental run with $G \approx 400$ kg/m^{2}s and $\Delta T_{sub,in} \approx 30$°C, which was susceptible to severe instability. The temporal spacing of each image sequence is selected to capture key flow features and is stated in each figure's caption, although the capture rate is maintained constant at 500 frames per second to observe high-frequency transients. Fig. 3 (a), depicts an image sequence with mild vapor production at a relatively low q''_w of 17.7 W/cm^2. Red arrows are included to highlight flow features pertinent to the discussion. The sequence begins with a large vapor patch exiting the channel. It is followed by another patch of vapor, which grows and accelerates as it slides along the heated wall. However, at 0.588 s, the flow begins to decelerate within the channel. Forward accelerating flow is resumed, and the vapor patch proceeds to exit the channel at 0.648 s. Subsequently, the indicated vapor patch in the remainder of the sequence accelerates downstream prior to decelerating around 0.718 s. Fig. 3 (b) shows the transient p_{in} signal surrounding the image sequence presented in Fig. 3 (a). p_{in} features minor and inconsistent fluctuations that are routinely observed during steady operation, caused by small perturbations of system components. Two local minima in p_{in} are highlighted at 0.576 and 0.736 s that occur during the period presented in Fig. 3 (a). The p_{in} minimums occur shortly before vapor deceleration is visually observed. The frequency of p_{in} fluctuations is shown in Fig. 3 (c), which contains the power spectrum by fast Fourier transform of the p_{in} signal during the final 120 seconds of the heating increment. The power spectrum shows the peak frequency of the oscillations is broadly spread between 3 and 9 Hz and the amplitude is relatively low. The frequency of the observed cyclic vapor deceleration is 7.7 Hz, corresponding to the 0.13 s between deceleration events, falls within the elevated frequencies of the p_{in} power spectrum. However, the spread of the frequencies hinders a distinct correlation between the two phenomena.

Fig. 4 replicates the format of Fig. 3 but features a higher q''_w of 25.2 W/cm^2. The instability is more prominent and vapor stagnation can be seen near the channel's outlet at 0.284 s in Fig. 4 (a). Forward flow resumes at 0.324 s and the vapor patches accelerate as they traverse the channel, until slowing down at 0.534 s. The oscillatory nature of p_{in} is more noticeable in Fig. 4 (b) compared to that at a lower q''_w, but still with some irregularities. Similar to Fig. 3, the flow deceleration visually observed at 0.324 and 0.534 s occurs near the local minima of p_{in} at 0.288 and 0.512 s, respectively. The local maxima of p_{in} at 0.352 s aligns with the vapor acceleration at 0.364 s. The clearer peaks are substantiated by the power spectrum, which depicts a distinct peak frequency around 4 Hz with an amplitude that is an order of magnitude larger than that at 17.7 W/cm^2.

Further increasing q''_w to 30.6 W/cm^2 intensifies the instability, resulting in a sinusoidal p_{in} signal with a peak frequency of 4 Hz, as observed in Figs. 5 (b) and 5 (c). At 0.382 s, p_{in} reaches a minimum, corresponding to the deceleration of flow in Fig. 5 (a). Albeit similar to Figs. 3 and 4, Fig. 5 shows more severe oscillations because of the higher q''_w. The more severe instability manifests as flow reversal near the outlet, which causes vapor to move towards the inlet at 0.414 s in Fig 5 (a). This is triggered by liquid backflow from the outlet that penetrates upstream into the channel, destroying vapor structures along the way, and causes a rise in p_{in}. Around 0.48 s, p_{in} reaches a local maximum and overcomes the inertia of back-flowing liquid, prompting flow to resume forwards. Flow boiling proceeds, vapor structures are reestablished, and p_{in} decreases until another minimum is reached at 0.638 s. The conclusion of the sequence, after p_{in} reaches a local minimum, shows the vapor along the wall decelerating at 0.654 s and reversing at 0.674 s as liquid backflows into the channel in the final image.

Fig. 6 illustrates additional transient measurements recorded during the same operating conditions as in Fig. 5, displaying severe instability. Figs. 6 (a-d) feature plots of p_{in}, pressure drop across the test section (Dp), $\dot{m}$, and accumulator displacement, respectively. An extended period of 30 seconds is presented to observe any low frequency variations in key parameters, which could be indicative of PDOs, as discussed in section 1.3. Assessing p_{in} over the extended duration reveals some deviations in the amplitude of high frequency oscillations. However, these inconsistencies are relatively minor compared to the rapid, large amplitude fluctuations that were observed at 4 Hz, as indicated by the distinct peak in Fig. 5 (c), which assesses frequencies over the entire 120-second steady period. In the presence of PDOs, long period, large amplitude, out-of-phase oscillations of Dp and $\dot{m}$ are expected. However, Fig. 6 (b) shows fluctuations in Dp are sporadic compared to variations in p_{in} and unaffected by the distinct fluctuations in $\dot{m}$ in Fig. 6 (c). While the $\dot{m}$ variations are clear, the amplitude is within 10% of the desired flow rate of 5 g/s, even during liquid backflow. It should be noted that the discrepancy in response time of the flow meter, at most 200 ms, and pressure transducers, at most 1 ms, would preclude a one-to-one comparison of signals near frequencies corresponding to the flow meter's response time, 5 Hz. However, both have sufficient response times to capture variations relative to PDOs, which are typically less than 1 Hz [57]. As illustrated in the flow loop in Fig. 2 (a), $\dot{m}$ is measured immediately downstream of the pump and may not accurately represent the $\dot{m}$ at each location along the loop. The stiffness provided by upstream components dampens the propagation of instability further upstream and the measured $\dot{m}$ is nearly constant. This is a limitation of the system which was designed for precise control during the collection of heat

Table 1
Summary of operating conditions of the present experiments in μg_e and g_e.

	ISS (μg_e)	Ground (g_e)
Mass velocity, G	199.9 – 2400.0 kg/m^{2}s	199.2 – 3200.0 kg/m^{2}s
Mass flow rate, $\dot{m}$	2.5 – 30.0 g/s	2.5 – 40.0 g/s
Inlet pressure, p_{in}	146.5 – 154.1 kPa	139.7 – 151.7 kPa
Inlet temperature, T_{in}	24.3 – 66.7°C	18.8 – 59.7°C
Inlet subcooling, $\Delta T_{sub,in}$	2.1 – 44.3°C	8.2 – 48.2°C
Inlet quality, $x_{e,in}$	-0.59 – -0.03	-0.64 – -0.11
Outlet pressure, p_{out}	145.5 – 153.6 kPa	133.7 – 149.4 kPa
Outlet temperature, T_{out}	31.6 – 68.6°C	19.8 – 69.0°C
Outlet subcooling, $\Delta T_{sub,out}$	0.0 – 36.9°C	0.0 – 46.5°C
Outlet quality, $x_{e,out}$	-0.49 – 0.08	-0.55 – 0.14
Wall heat flux, q''_w	4.3 – 47.6 W/cm^2	5.5 – 49.3 W/cm^2
Number of data points, N	154	186

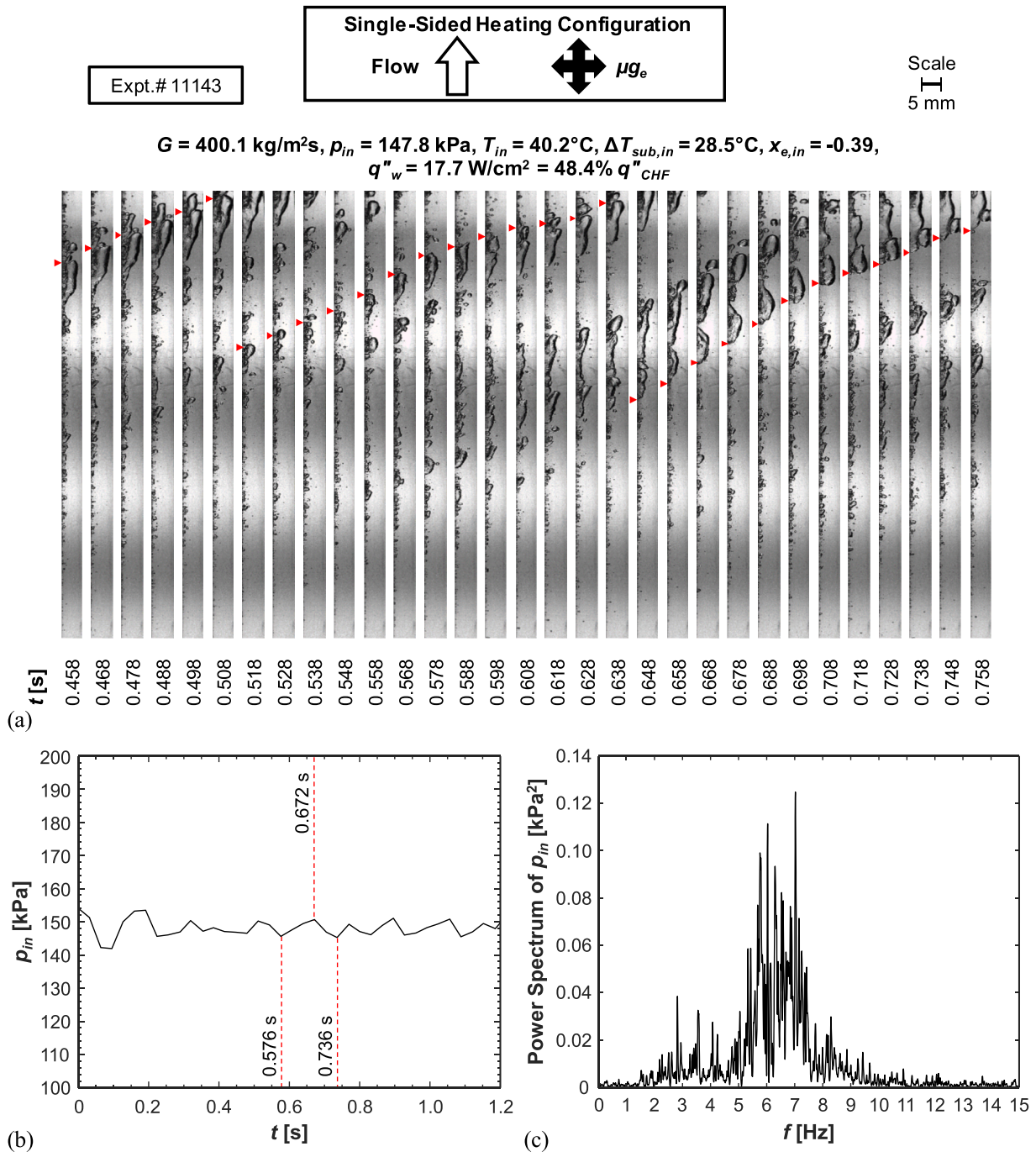

Fig. 3. (a) Flow visualization image sequence tracking motion within the channel during a mass velocity of $G \approx 400$ kg/m^{2}s, inlet subcooling of $\Delta T_{sub,in} \approx 30$°C, and heat flux of $q''_w = 17.7$ W/cm^2 = 48.4% q''_{CHF} in microgravity. Time interval between successive images is 0.01 s. Corresponding (b) temporal plot of inlet pressure surrounding the image sequence, and (c) power spectrum by fast Fourier transform of the inlet pressure during the final 120 s of the heating increment.

transfer and CHF data and not optimized to study instabilities. However, compared to the dynamics observed within the channel, the measured variations in $\dot{m}$ near the pump have a minor effect on p_{in} oscillations. Similarly, the variations in $\dot{m}$ provided by the pump are relatively insignificant to the displacement of the accumulator in Fig. 6 (d). The accumulator's displacement is a measure of the expansion and contraction of bellows in response to variations in the pressure difference between the nPFH-side and airside of the accumulator. For all cases in the present study, the airside pressure is relatively steady, therefore the accumulator displacement variations are caused by fluctuations on the nPFH-side. The p_{in} oscillations propagate downstream, and the accumulator displacement features oscillations resembling those of p_{in}. However, the oscillation amplitude is less than 0.5 mm, *i.e.*, less than 0.3% of total displacement, and the accumulator position is relatively steady. This is negligible compared to p_{in} oscillations, which can reach 40% of the mean p_{in}.

3.2. Comparison of Instabilities at Various Operating Conditions

During the primary FBCE experiments, it was evident $\Delta T_{sub,in}$ affected stability. Severe instability was exclusive to high $\Delta T_{sub,in}$, such as that presented in the previous subsection. An image sequence recorded during a low subcooling case where $G = 800.0$ kg/m^{2}s, $\Delta T_{sub,in} = 9.1$°C, and $q''_w = 19.0$ W/cm^2, is presented in Fig. 7 (a). No instabilities

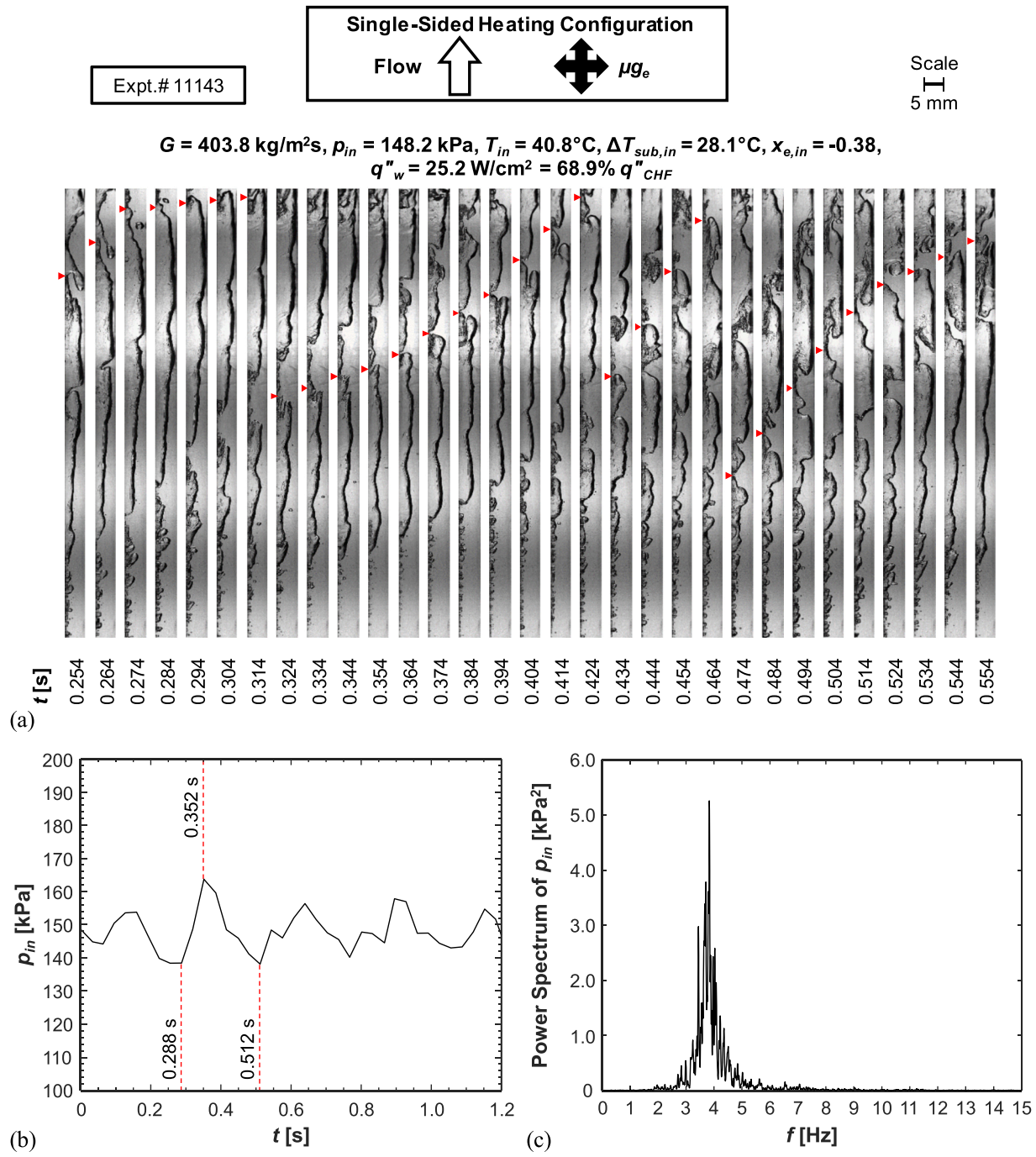

Fig. 4. (a) Flow visualization image sequence tracking motion within the channel during a mass velocity of $G \approx 400$ kg/m^{2}s, inlet subcooling of $\Delta T_{sub,in} \approx 30$°C, and heat flux of $q''_w = 25.2$ W/cm^2 = 68.9% q''_{CHF} in microgravity. Time interval between successive images is 0.01 s. Corresponding (b) temporal plot of inlet pressure surrounding the image sequence, and (c) power spectrum by fast Fourier transform of the inlet pressure during the final 120 s of the heating increment.

or unusual flow patterns are visually apparent. Flow visualization reveals stable flow in the channel, which corresponds to a relatively steady p_{in} in Fig. 7 (b). This is reflected in Fig. 7 (c) by a power spectrum with a dispersed peak and low amplitudes, indicative of random fluctuations.

An increased subcooling is depicted in Fig. 8, with $G = 800.1$ kg/m^{2}s, $\Delta T_{sub,in} = 19.2$°C, and $q''_w = 18.3$ W/cm^2. In contrast to the lower subcooling in Fig. 7, the oscillations are more pronounced and exhibit a distinct peak frequency around 9 Hz, with a spread between 7 and 10 Hz, in Figs. 8 (b) and 8 (c), respectively. Furthermore, a periodic pattern is observed in Fig. 8 (a), where a thin, long, continuous bubble forms along the heated wall at 0.735, 0.835, and 0.955 s. The bubbles traverse the channel and are replaced by shorter discrete vapor patches on the wall. The formation of long bubbles occurs at 0.703, 0.799, 0.928 s, approximately 0.03s after each p_{in} minimum.

Fig. 9 (a) contains an image sequence with $G = 800.0$ kg/m^{2}s, $\Delta T_{sub,in} = 29.5$°C, and $q''_w = 17.7$ W/cm^2. The elevated $\Delta T_{sub,in}$ requires more heat to bring the near-wall fluid to T_{sat} and increases the potential for condensation. This results in significantly less vapor within the channel compared to cases with lower $\Delta T_{sub,in}$. The image sequence reveals bubbles randomly nucleate along the heated wall, grow slightly, and condense before they detach or coalesce. The flow remains stable and yields a relatively steady p_{in}, as shown in Fig. 9 (b). However, a distinct frequency around 9.5 Hz is detected in Fig. 9 (c), contradicting the observed flow patterns. Analyzing the pressure fluctuations around the

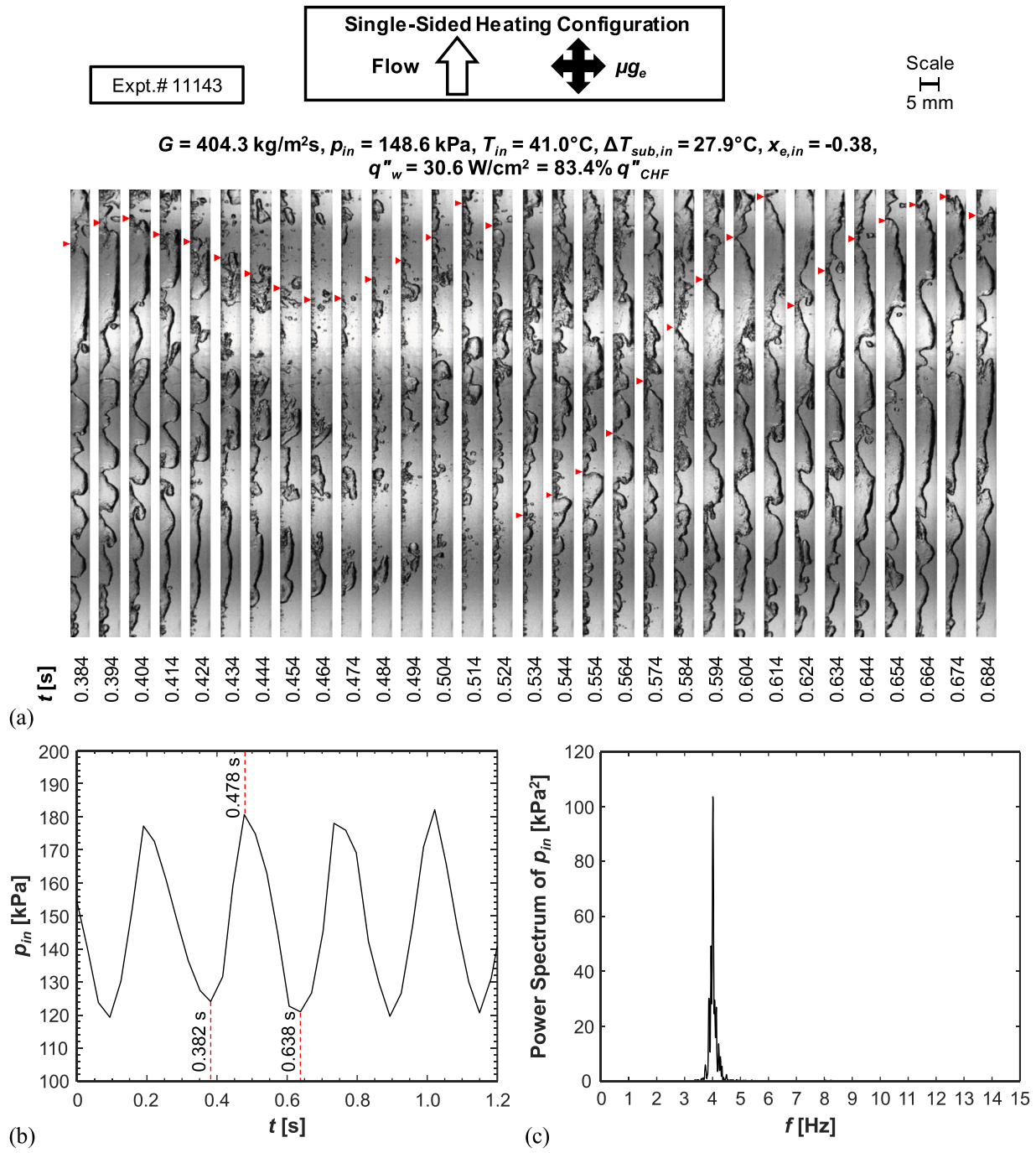

Fig. 5. (a) Flow visualization image sequence tracking motion within the channel during a mass velocity of $G \approx 400$ kg/m^{2}s, inlet subcooling of $\Delta T_{sub,in} \approx 30$°C, and heat flux of $q''_w = 30.6$ W/cm^2 = 83.4% q''_{CHF} in microgravity. Time interval between successive images is 0.01 s. Corresponding (b) temporal plot of inlet pressure surrounding the image sequence, and (c) power spectrum by fast Fourier transform of the inlet pressure during the final 120 s of the heating increment.

loop reveals the p_{in} fluctuations are not a result of flow transients in the test section but are induced by the pump. The power spectrum of the pump's outlet pressure, $p_{pump,out}$, is presented in Fig. 9 (d), revealing an identical peak frequency with greater amplitude than that of p_{in}. In the absence of significant vapor production, minor pump-induced vibrations become more prominent when analyzing the frequency composition of p_{in}. However, these minor fluctuations do not impact the observed flow patterns.

To summarize, it is difficult to ascertain the effects of $\Delta T_{sub,in}$ on instability from Figs. 7-9. Low $\Delta T_{sub,in}$ precluded instabilities in Fig. 7. In Fig. 8, with a higher $\Delta T_{sub,in}$, minor fluctuations in p_{in} corresponded to slight variations in flow patterns. Further increasing $\Delta T_{sub,in}$, at similar G and q''_w, suppressed vapor production and eliminated any instabilities in Fig. 9. This suggests large $\Delta T_{sub,in}$ effectively eliminates instabilities. However, the most severe instabilities were observed at the combination of high $\Delta T_{sub,in}$ and high q''_w. To compare different operating conditions at analogous points on the boiling curve, trends are compared at similar percentages of CHF, % q''_{CHF} instead of q''_w. Even though the present set of experiments were stopped prior to CHF, q''_{CHF} is estimated from the corresponding operating conditions in the consolidated FBCE-CHF database [28]. Flow stability at $\Delta T_{sub,in} \approx 20$°C and 30°C is revisited at $q''_w \approx 80\%$ q''_{CHF}, matching Fig. 7.

Fig. 10 (a) shows an image sequence for the same case as Fig. 8, but at a higher q''_w of 21.5 W/cm^2 = 79.3% q''_{CHF}. For this case, the increase in

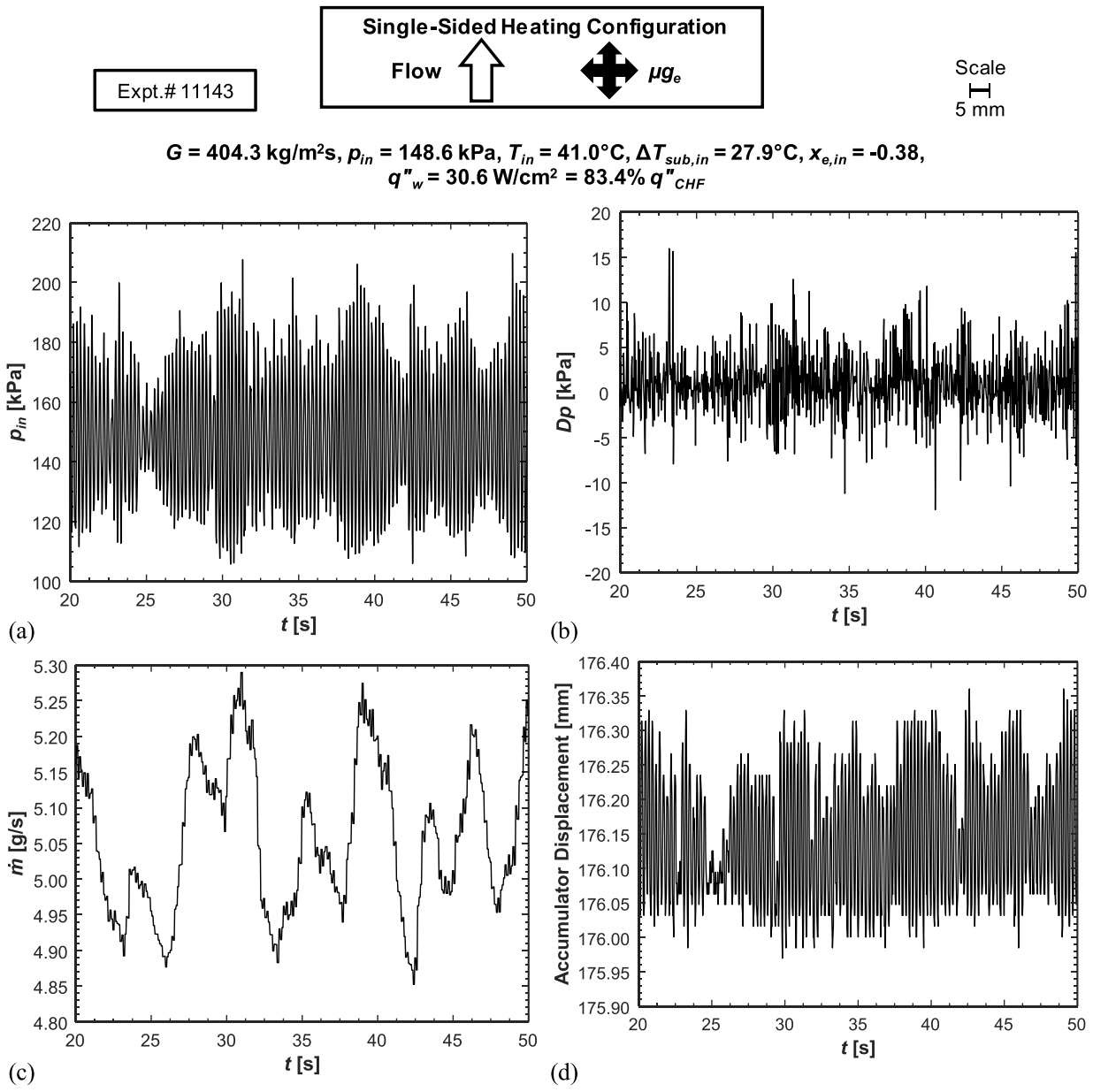

Fig. 6. Temporal plots of (a) inlet pressure, (b) pressure drop across the FBM's heated length, (c) mass flow rate, and (d) accumulator displacement/level over a period of 30 s during a mass velocity of $G \approx 400$ kg/m^{2}s, inlet subcooling of $\Delta T_{sub,in} \approx 30$°C, and heat flux of $q''_w = 30.6$ W/cm^2 = 83.4% q''_{CHF} in microgravity.

q''_w was moderate and discussion regarding the observed flow transients of p_{in} in Fig. 8 still applies. Noteworthy differences between Figs. 10 and 8 are the thicker vapor structures, larger amplitude fluctuations, and lower peak frequency in Fig. 10. Similarly, the instability is more pronounced and the peak frequency's amplitude of the power spectrum is an order of magnitude higher than that at the lower $\Delta T_{sub,in}$ in Fig. 7.

Fig. 11 features $\Delta T_{sub,in} \approx 30$°C and $q''_w = 80.5\%\ q''_{CHF}$, which is considerably higher than that in Fig. 9, $q''_w = 41.2\%\ q''_{CHF}$. Unlike Fig. 9, the image sequence in Fig. 11 (a) shows nucleation in the channel's upstream region and a noticeable thickening of the vapor layer along the channel. Instability is apparent at 0.626 s where, shortly after the local p_{in} minimum in Fig. 11 (b), liquid backflows into the channel, collapsing vapor in its wake. Flow boiling resumes in the forward direction and proceeds until a second surge of backflow is observed at 0.846 s. The duration between the occurrences of backflow is 0.22 s, which corresponds to the peak frequency of the p_{in} power spectrum, ~4.5 Hz, as shown in Fig. 11 (c). Instability becomes visually more apparent at high $\Delta T_{sub,in}$ and is reflected in p_{in}. The transient p_{in} signal displays a sinusoidal pattern in Fig. 11 (b), and the peak frequency of the power spectrum has an amplitude of 9.4 kPa^2 in Fig. 11 (c). At lower $\Delta T_{sub,in}$, Figs. 7 and 10, the peaks of the power spectrum were more dispersed with magnitudes less than 1 kPa^2.

Thus far, the most intense instabilities occurred at $\Delta T_{sub,in} \approx 30$°C and $q''_w \approx 80\%\ q''_{CHF}$ with $G = 404.3$ and 803.6 kg/m^{2}s, as depicted in Figs. 5 and 11, respectively. At both G, p_{in} oscillations occur at a distinct frequency, which corresponds to liquid backflow from the outlet. The peak frequency of the power spectrum is marginally lower, and the amplitude is significantly larger, albeit spread out over a wider range of frequencies, at $G = 404.3$ kg/m^{2}s. This is attributed to the stronger forward inertia of the flow more easily overcoming liquid backflow at $G = 803.6$ kg/m^{2}s, thereby reducing the instability's magnitude.

3.3. Comparison of Instabilities in Microgravity to Vertical Upflow in Earth Gravity

Instabilities manifested differently in μg_e compared to vertical

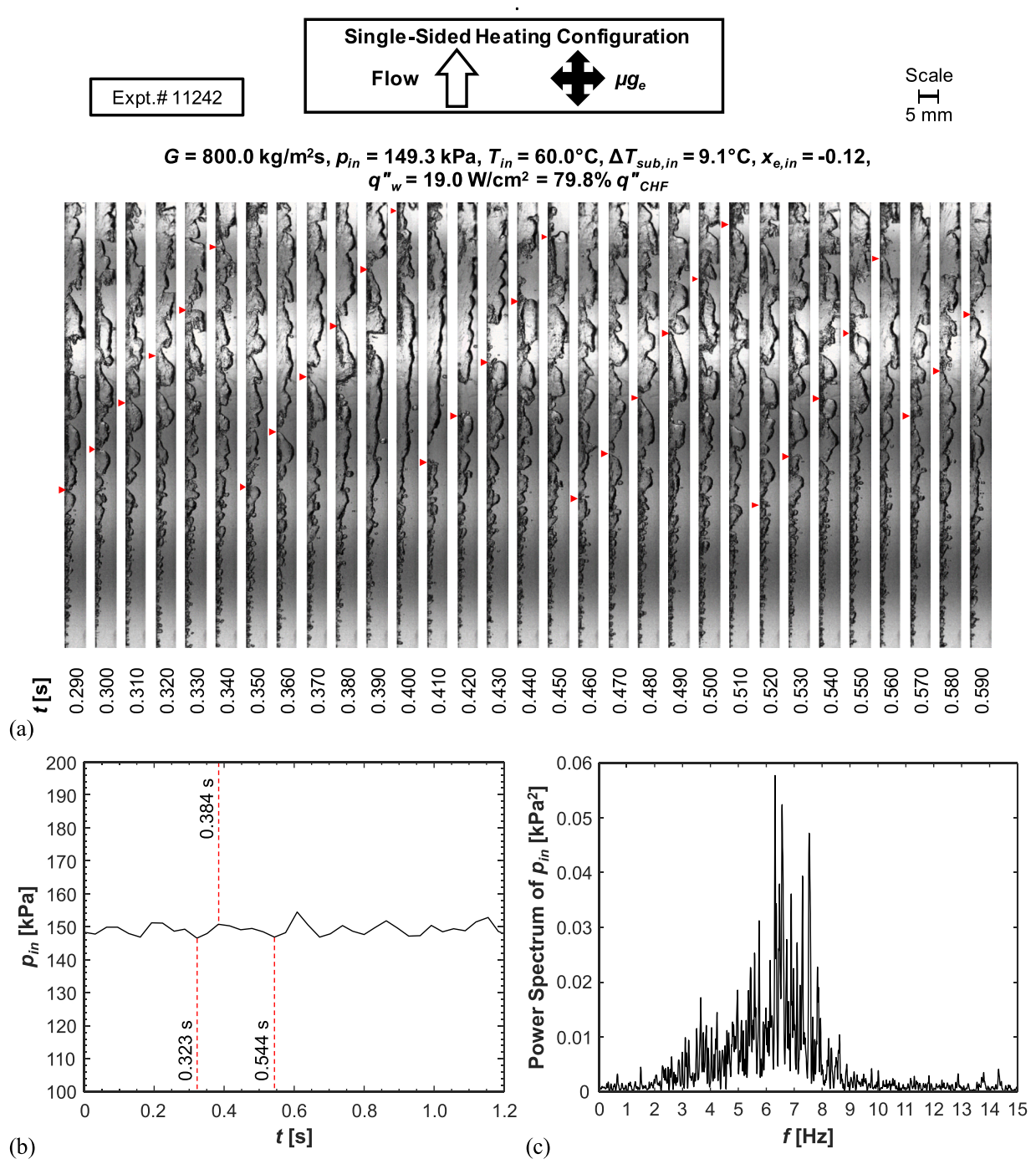

Fig. 7. (a) Flow visualization image sequence tracking motion within the channel during mass velocity of $G \approx 800$ kg/m^{2}s, inlet subcooling of $\Delta T_{sub,in} \approx 10$°C, and heat flux of $q''_w = 19.0$ W/cm^2 = 79.8% q''_{CHF} in microgravity. Time interval between successive images is 0.01 s. Corresponding (b) temporal plot of inlet pressure surrounding the image sequence, and (c) power spectrum by fast Fourier transform of the inlet pressure during the final 120 s of the heating increment.

upflow in g_e. Instabilities are prominent at low G, which coincides with when the influence of body force is most significant. Fig. 12 (a) features an image sequence with $G = 204.0$ kg/m^{2}s, $\Delta T_{sub,in} = 30.3$°C, and $q''_w = 22.7$ W/cm^2 = 90.8% q''_{CHF} in μg_e. At low G, liquid backflow is relatively weak and vapor structures within the channel remain intact. Despite this, clear backflow is observed in the channel. At 0.693 s, flow begins to stagnate as reversal starts downstream, drifts forward slightly, completely reversing at 0.753 s. A second period of reversal begins downstream at 0.943 s, corresponding to a frequency of 4 Hz. Figs. 12 (b) and 12 (c) show a sinusoidal p_{in} signal and power spectrum with a clear peak frequency, characteristic of flow reversal.

Fig. 13 illustrates results with similar operating conditions, $G = 199.8$ kg/m^{2}s, $\Delta T_{sub,in} = 27.8$°C, and $q''_w = 27.4$ W/cm^2 = 88.7% q''_{CHF} but during vertical upflow in g_e. The image sequence in Fig. 13 (a) with a 0.02 s interval between consecutive images, as well as all other cases in g_e, has no flow reversal. Flow boiling is relatively stable and vapor patches grow as they slide along the wall, which is a source of minor instability. During vertical upflow in g_e, buoyancy augments vapor acceleration, increasing both slip velocity and interfacial shear stress. In extreme cases, the slower-moving liquid impedes the faster-moving vapor, causing some disturbances. This occurs at the beginning of the sequence in Fig. 13 (a). A thick vapor structure spanning the height of

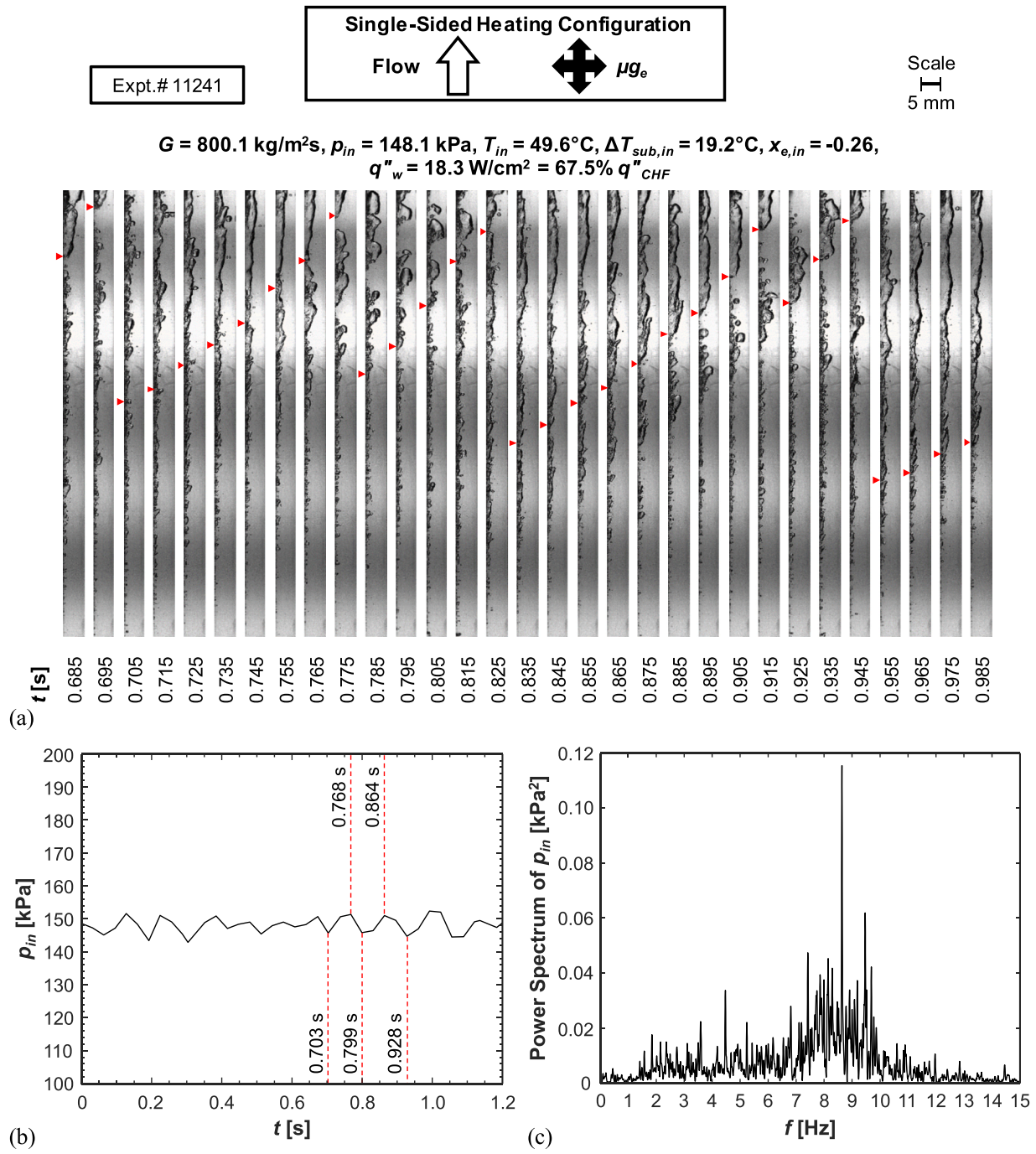

Fig. 8. (a) Flow visualization image sequence tracking motion within the channel during a mass velocity of $G \approx 800$ kg/m^{2}s, inlet subcooling of $\Delta T_{sub,in} \approx 20$°C, and heat flux of $q''_w = 18.3$ W/cm^2 = 67.5% q''_{CHF} in microgravity. Time interval between successive images is 0.01 s. Corresponding (b) temporal plot of inlet pressure surrounding the image sequence, and (c) power spectrum by fast Fourier transform of the inlet pressure during the final 120 s of the heating increment.

the channel is indicated in the first image. In the second image, the same vapor structure is barely recognizable due to interfacial shear slowing the vapor near the adiabatic wall, deforming the large vapor structures, and promoting mixing with the subcooled liquid, which leads to condensation. The next patch of vapor being tracked at 0.634 s, grows unimpeded within the channel. However, as it accelerates, it merges with downstream vapor that was slowed by the liquid. The conglomerated vapor occupies most of the channel and is further decelerated by prominent interfacial shear. Regardless of the disturbances observed in the image sequence, the flow is mostly stable, p_{in} is relatively constant, and the power spectrum features random low amplitude spikes spanning 1.5 – 5 Hz.

4. Experimental Results and Discussion

4.1. Quantification of Instability

Visual inspection of flow stability, as presented in section 3, showed instabilities manifest as irregularities of vapor motion within the channel. The severity of instability is contingent on the operating conditions and ranges from alternating acceleration and deceleration of vapor as it slides along the wall to backflow of liquid into the channel. Conversely, the vapor layer continually accelerates as it slides along the wall during stable flow, as shown in Figs. 7 and 9. The entire catalog of flow visualization was thoroughly assessed to identify operating conditions that

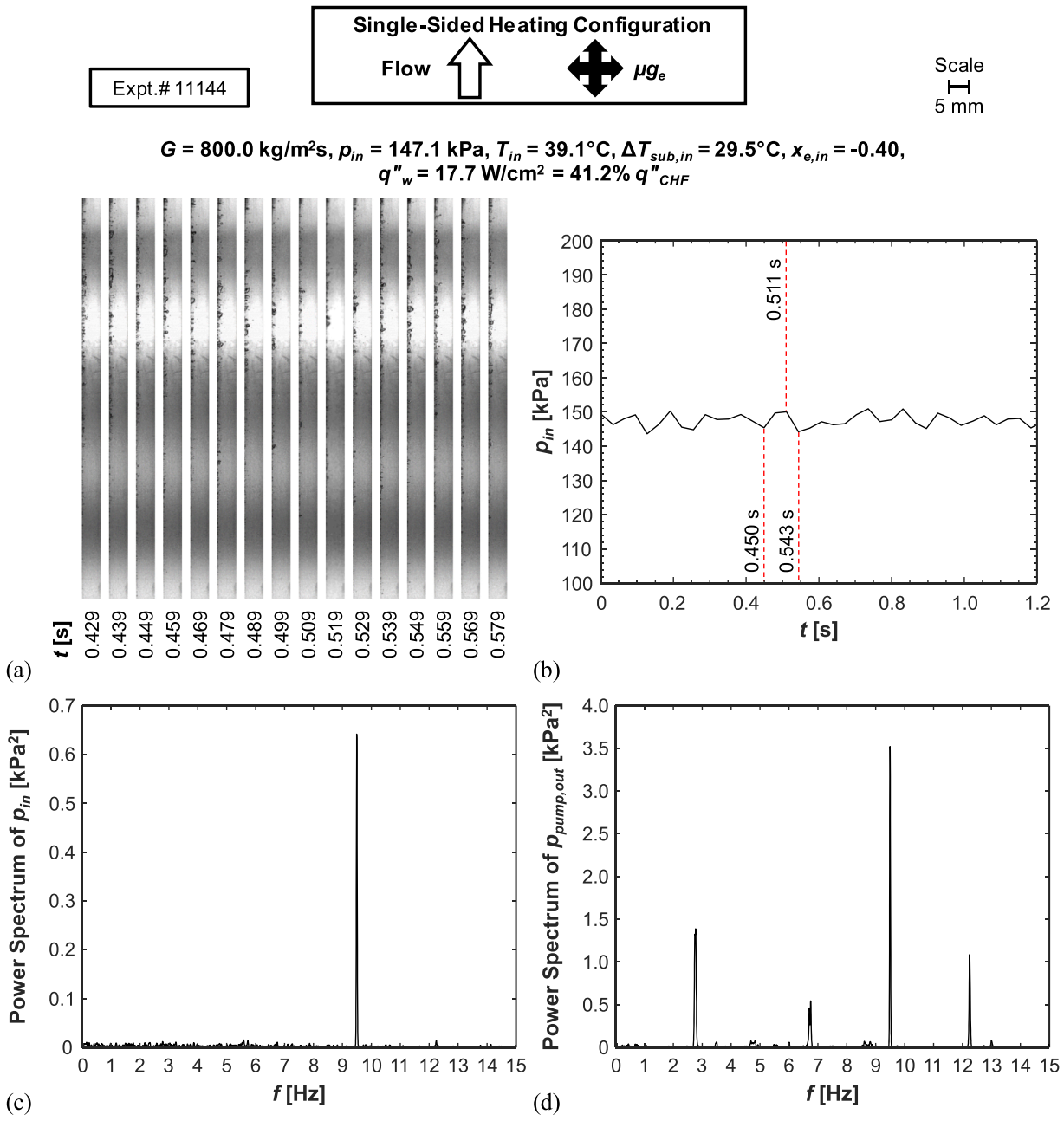

Fig. 9. (a) Flow visualization image sequence tracking motion within the channel during a mass velocity of $G \approx 800$ kg/m^{2}s, inlet subcooling of $\Delta T_{sub,in} \approx 30$°C, and heat flux of $q''_w = 17.7$ W/cm^2 = 41.2% q''_{CHF} in microgravity. Time interval between successive images is 0.01 s. Corresponding (b) temporal plot of inlet pressure surrounding the image sequence, and power spectrum by fast Fourier transform of the (c) inlet pressure and (d) pump outlet pressure during the final 120 s of the heating increment.

exemplified instability.

A subset of the database at high $\Delta T_{sub,in}$ and low q''_w, near ONB, exhibited pulsing bubble growth and significant p_{in} fluctuations. Fig. 14 depicts an image sequence with 0.002 s between consecutive images, wherein high frequency bubble growth and collapse occur along the heated wall. This pulsing behavior is presumed to induce p_{in} fluctuations. The frequency of this phenomenon is visually ~60 Hz, whereas the data sampling rate is 30 Hz, preventing its accurate capture. Reliable conclusions cannot be inferred from this data, and it is excluded from further analysis. Additional exclusions include the heating increments prior to and including ONB and the increment when the experiment is terminated, either manually or by CHF detection.

The remaining portion of the database was classified as either stable or unstable based on available flow visualization. Statistical parameters that quantify the fluctuations of transient measurements around the loop of pressure, temperature, flow rate and accumulator displacement were calculated. For a measurement φ, these parameters include the range ($\Delta\varphi$), mean deviation (φ_{MD}), mean absolute deviation (φ_{MAD}), standard deviation (φ_{STD}), and variance (φ_{VAR}), defined respectively as

$$\Delta\varphi = \varphi_{max} - \varphi_{min}, \tag{6}$$

$$\varphi_{MD} = \frac{\sum_{i=1}^{N} (\varphi_i - \overline{\varphi})}{N}, \tag{7}$$

$$\varphi_{MAD} = \frac{\sum_{i=1}^{N} |\varphi_i - \overline{\varphi}|}{N}, \tag{8}$$

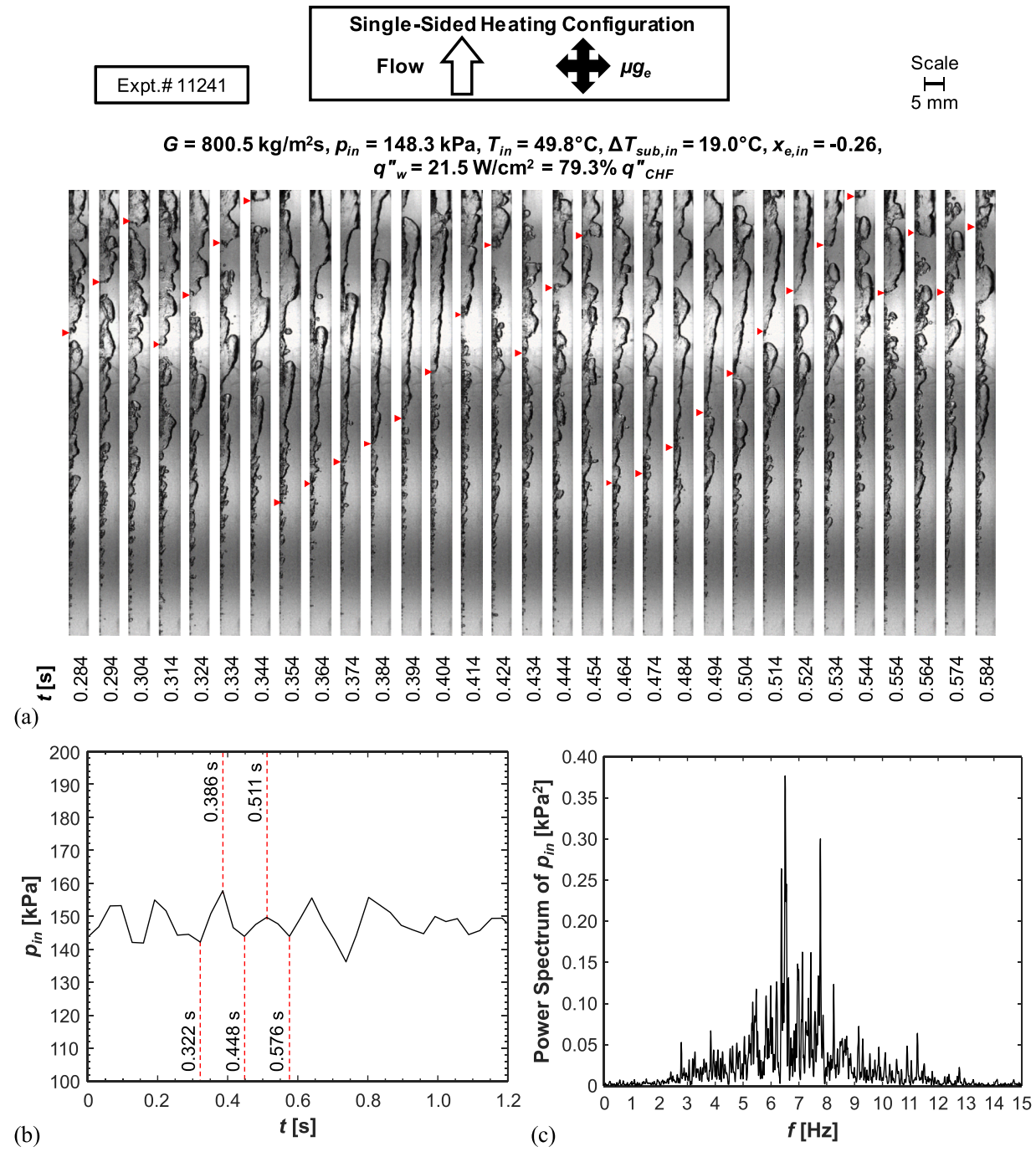

Fig. 10. (a) Flow visualization image sequence tracking motion within the channel during a mass velocity of $G \approx 800$ kg/m^{2}s, inlet subcooling of $\Delta T_{sub,in} \approx 20$°C, and heat flux of $q''_w = 21.5$ W/cm^2 = 79.3% q''_{CHF} in microgravity. Time interval between successive images is 0.01 s. Corresponding (b) temporal plot of inlet pressure surrounding the image sequence, and (c) power spectrum by fast Fourier transform of the inlet pressure during the final 120 s of the heating increment.

$$\varphi_{STD} = \sqrt{\frac{\sum_{i=1}^{N}(\varphi_i - \overline{\varphi})^2}{N-1}}, \text{and} \tag{9}$$

$$\varphi_{VAR} = \frac{\sum_{i=1}^{N}(\varphi_i - \overline{\varphi})^2}{N-1}. \tag{10}$$

A Chi-Square feature ranking algorithm is implemented in MATLAB [58] to identify the parameters exhibiting a strong correlation with instability. The statistics of various pressure measurements within the FBM and upstream of the heated length yielded the smallest *p-values*, indicating statistical significance to the presence of instability. Although the pressure statistics offer insights into the flow's stability, a definitive cut-off value distinguishing stable and unstable flow could not be identified using any of the upstream pressure statistics. For instance, high flow rates inherently produce larger p fluctuations, leading to misclassification while relying solely on p. As referenced in section 1.3, DWOs are facilitated by different propagation speeds in the single- and two-phase regions. Taking inspiration from the intensity of a sound wave in a single-phase fluid [59], a *pseudo-intensity* of the pressure fluctuations is defined as

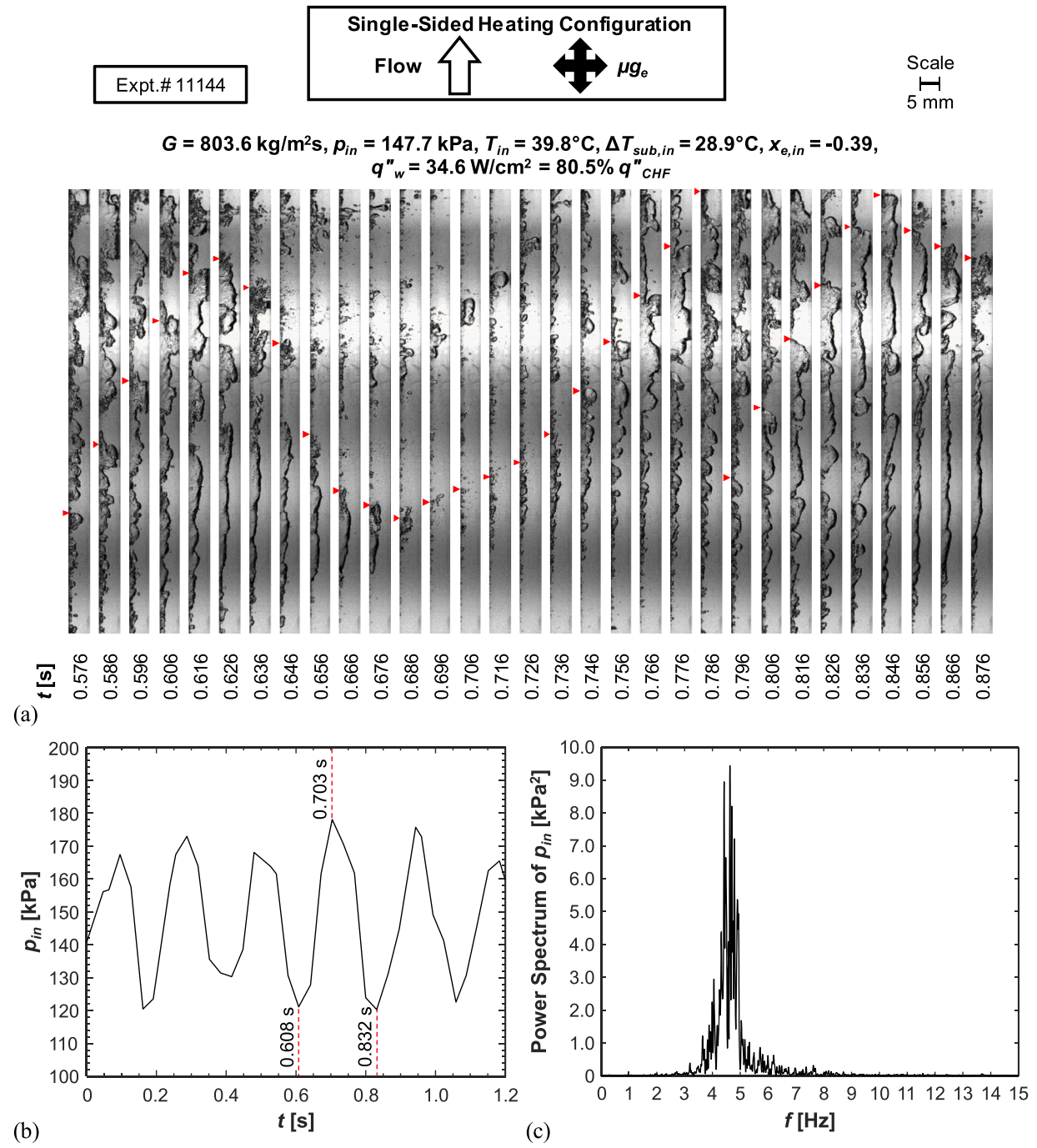

Fig. 11. (a) Flow visualization image sequence tracking motion within the channel during a mass velocity of $G \approx 800$ kg/m^{2}s, inlet subcooling of $\Delta T_{sub,in} \approx 30$°C, and heat flux of $q''_w = 34.6$ W/cm^2 = 80.5% q''_{CHF} in microgravity. Time interval between successive images is 0.01 s. Corresponding (b) temporal plot of inlet pressure surrounding the image sequence, and (c) power spectrum by fast Fourier transform of the inlet pressure during the final 120 s of the heating increment.

$$I = \frac{\Delta p^2}{2G}, \tag{11}$$

where Δp is the range of the pressure signal. A distinct transition from stable to unstable flow occurs and vapor motion becomes disrupted when I exceeds 1.8×10^5 W/m^2.

4.2. Experimental Trends of Instability

Fig. 15 examines various characteristics of p_{in} fluctuations during instabilities, $I > 1.8 \times 10^5$ W/m^2. Trends are assessed with respect to both phase change number, N_{pch}, and subcooling number, N_{sub}, which are commonly used in flow boiling instability studies. Figs. 15 (a) and 15 (b) depict variations of I with N_{pch} in μg_e and g_e during vertical upflow, respectively. In some cases, a large spread in I is observed in μg_e for specific combinations of N_{sub} and N_{pch} due to substantial differences in G and q''_w. Typically, I increases exponentially with N_{pch} in μg_e, as indicated by the logarithmic y-axis scale. I similarly increases with N_{pch} in g_e, but the maximum observed I is considerably lower than in μg_e. At the combination of high N_{sub} and N_{pch}, I exceeds 1×10^7 in μg_e, but the maximum I in g_e is 2.6×10^6. As discussed in Section 3.3, no backflow was observed in g_e, resulting in lower I, particularly at high N_{pch} where I is nearly constant or even decreases.

Figs. 15 (a) and 15 (b) presented trends of I, which captures the

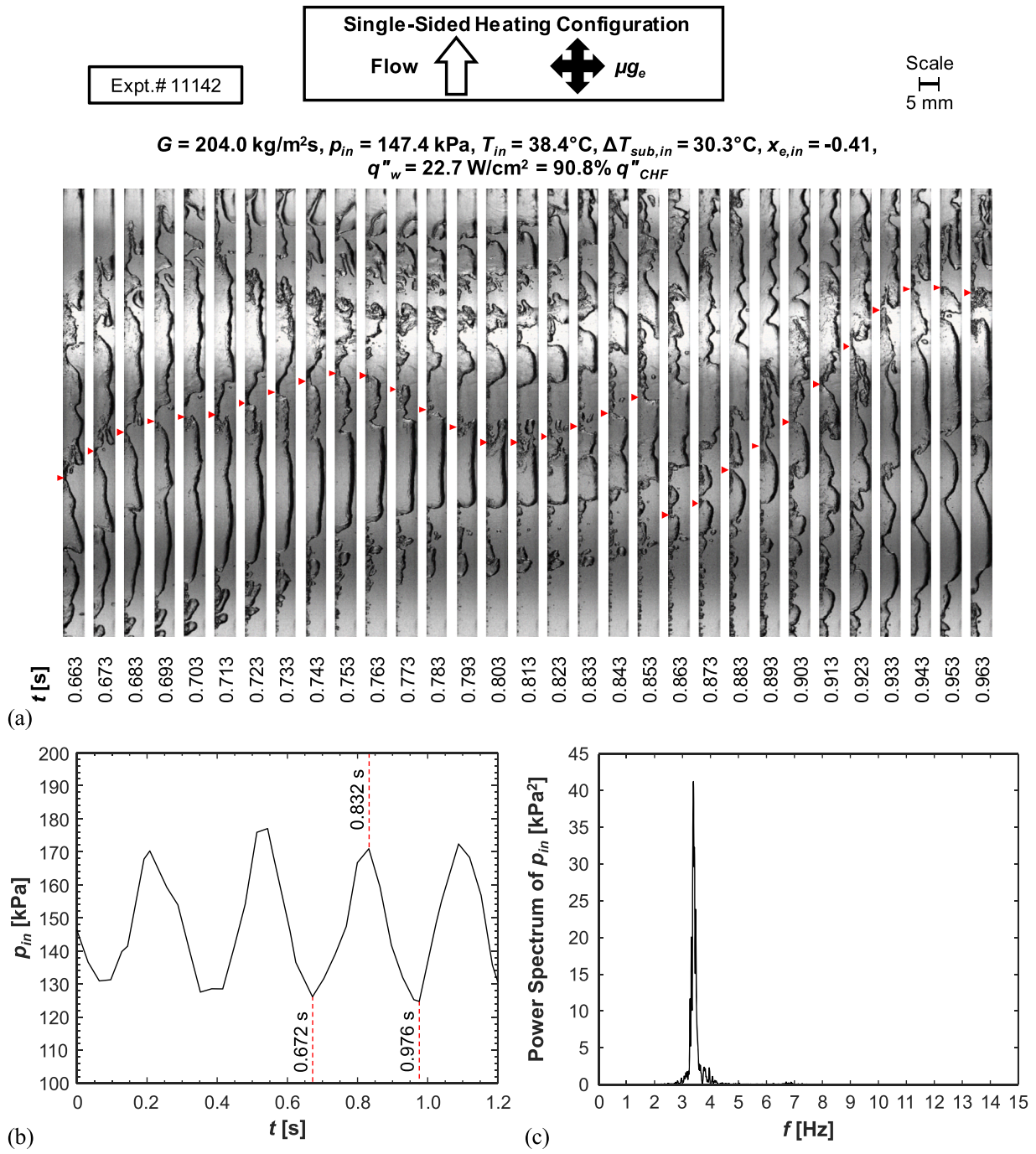

Fig. 12. (a) Flow visualization image sequence tracking motion within the channel during a mass velocity of $G \approx 200$ kg/m^{2}s, inlet subcooling of $\Delta T_{sub,in} \approx 30$°C, and heat flux of $q''_w = 22.7$ W/cm^2 = 90.8% q''_{CHF} in microgravity. Time interval between successive images is 0.01 s. Corresponding (b) temporal plot of inlet pressure surrounding the image sequence, and (c) power spectrum by fast Fourier transform of the inlet pressure during the final 120 s of the heating increment.

overall magnitude of the fluctuations relative to the flow's inertia. The peak frequency, f_{peak}, of the fluctuations and its respective amplitude, shown respectively in Figs. 15 (c) and 15 (e), are evaluated using the power spectrum of p_{in} during the final 120 seconds of the heating increment. In μg_e, f_{peak} decreases with N_{pch} but is independent of N_{sub}. As presented in section 3, instabilities at low G and high q''_w, corresponding to high N_{pch}, manifested as liquid backflow into the channel. At high N_{pch}, the weak forward inertia of the flow requires additional time to build sufficient p_{in} to overcome the liquid backflow, resulting in lower f_{peak}. At low $\Delta T_{sub,in}$ and relatively low q''_w, instabilities were minor, resulting in unclear amplitude trends at low N_{sub} and N_{pch}. However, the amplitude increases with N_{pch} at high N_{pch} at high N_{sub}, where backflow is prevalent.

Figs. 15 (d) and 15 (f) illustrate f_{peak} and its amplitude during vertical upflow in g_e. Compared to μg_e, instabilities were relatively minor in g_e, and the maximum power spectrum amplitude was 3.2 kPa^2. However, amplitude variations in g_e were relatively small with no distinct trend, unlike in μg_e where amplitude grew with N_{pch}, resulting in a maximum amplitude of 256.9 kPa^2. Similarly, f_{peak} varied significantly less in g_e than in μg_e, specifically at low N_{pch}. However, as presented in Fig. 13, f_{peak} is less distinct in g_e, and the frequency spectrum appears noisier, possibly precluding the identification of a true f_{peak} like that observed in μg_e.

To summarize, the studied instability produces p_{in} oscillations with a

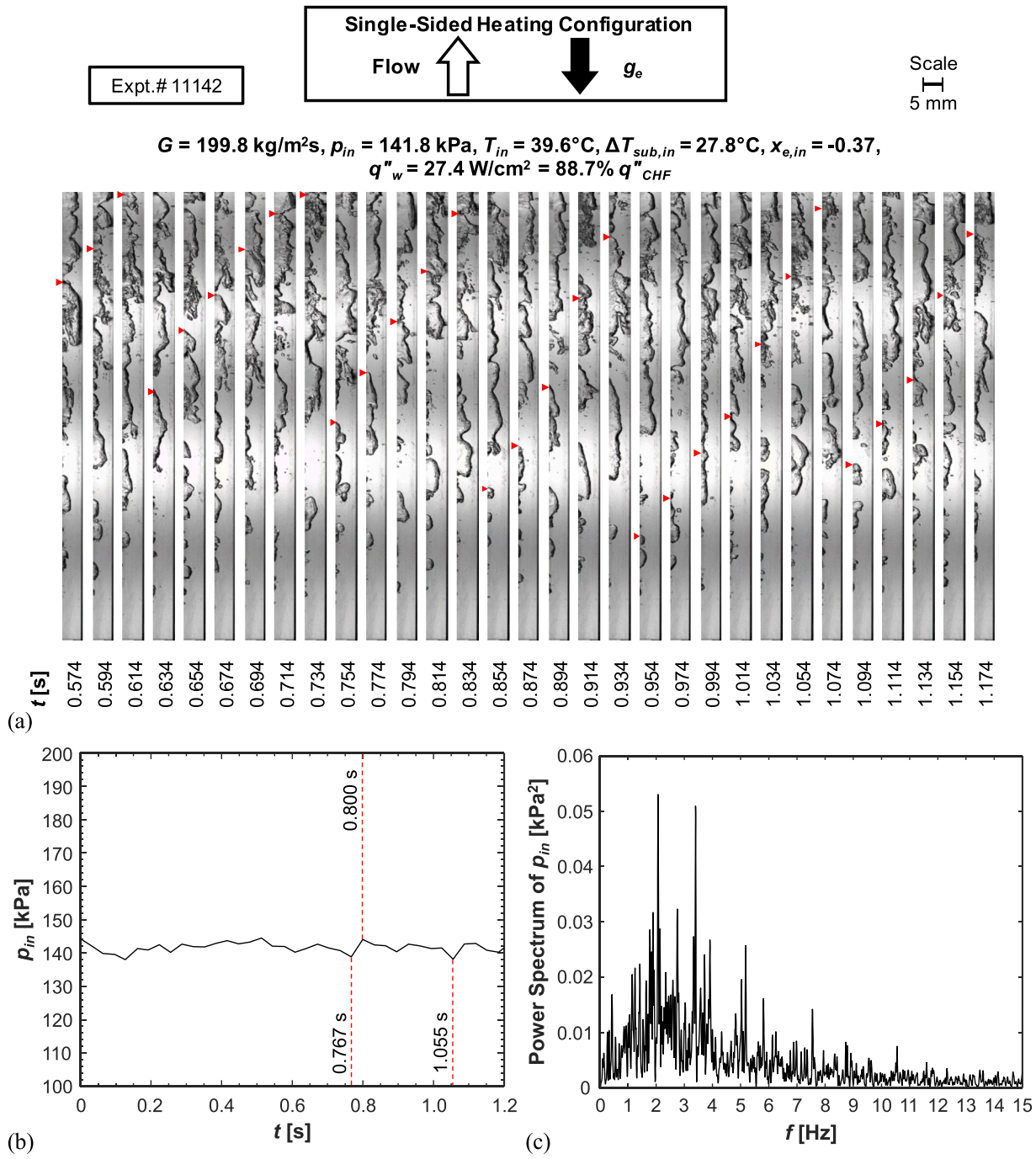

Fig. 13. (a) Flow visualization image sequence tracking motion within the channel during a mass velocity of $G \approx 200$ kg/m^{2}s, inlet subcooling of $\Delta T_{sub,in} \approx 30$°C, and heat flux of $q''_w = 27.4$ W/cm^2 = 88.7% q''_{CHF} in Earth gravity. Time interval between successive images is 0.02 s. Corresponding (b) temporal plot of inlet pressure surrounding the image sequence, and (c) power spectrum by fast Fourier transform of the inlet pressure during the final 120 s of the heating increment.

frequency exceeding 1 Hz and varying amplitude. Frequencies in this range are typically associated with DWOs, as opposed to PDOs which consist of low frequency, large amplitude, oscillations of *Dp* and $\dot{m}$. The observed instability fundamentally differs from PDOs and produces high frequency variations in p_{in}, but random fluctuations in *Dp* that are disconnected from $\dot{m}$, as shown in Fig. 6. However, effects of the instability are transferred throughout the flow loop, which could suggest a system-level instability. Fig. 16 examines the frequency and magnitude of pressure fluctuations at each pressure measurement location in the loop for the same operating conditions investigated in Figs. 5 and 6. The top row of plots displays pressure measurements upstream of the FBM, including pump inlet, pump outlet, and BHM inlet. The middle row consists of the four pressure measurements within the FBM, but upstream of the heated length, including the heated-length inlet pressure, p_{in}. The bottom row contains the remaining pressure measurements downstream of the heated length, including the heated length outlet, condenser outlet, and accumulator air-side pressure. Key observations of the pressure fluctuations around the loop are:

(i) Frequency of pressure fluctuations is consistent throughout the loop.
(ii) Magnitude of pressure fluctuations within the FBM, both upstream and downstream of the heated length, are nearly identical and is the maximum in the flow loop.

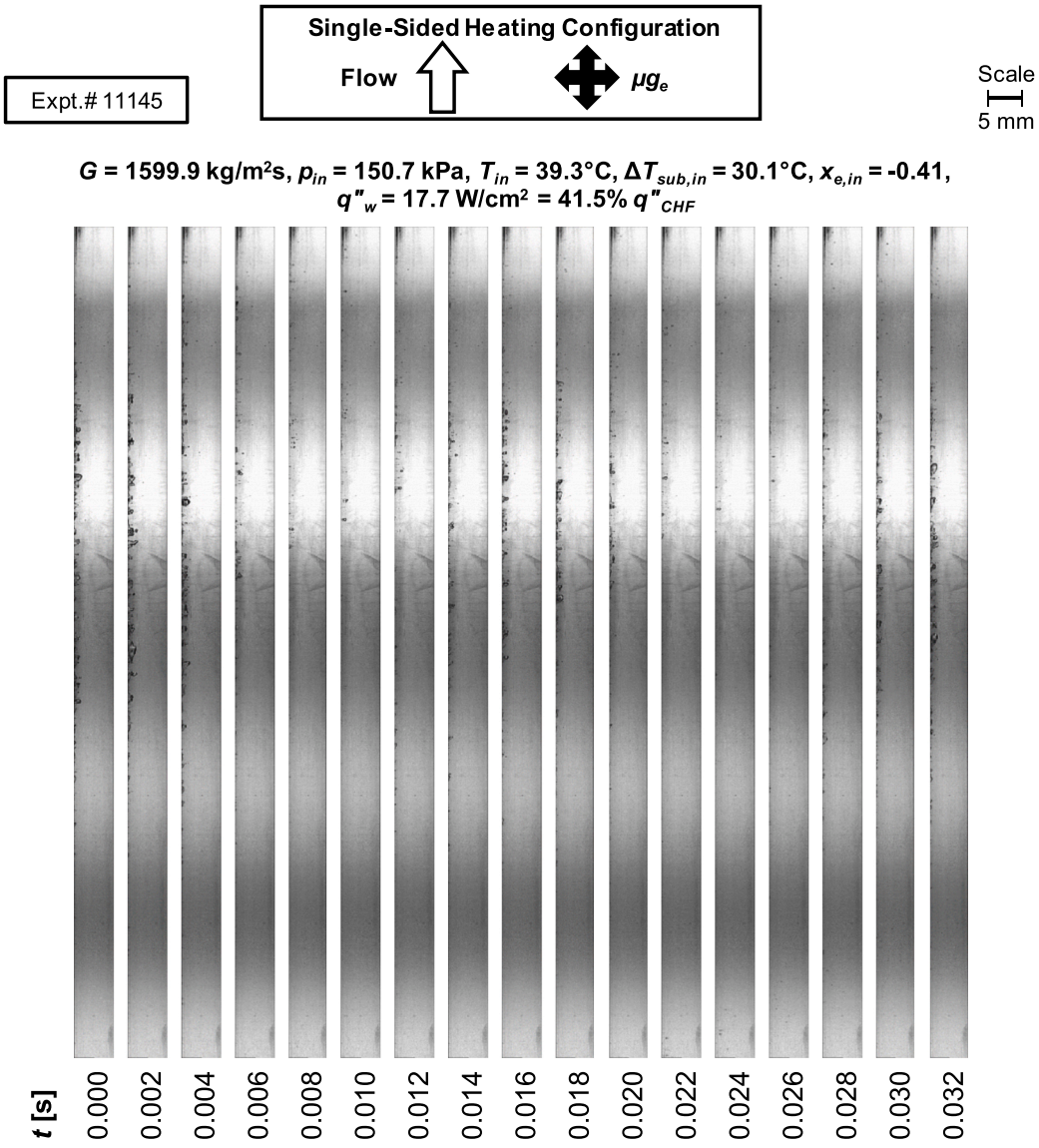

Fig. 14. Flow visualization image displaying cyclic bubble growth and collapse within the channel during mass velocity of $G \approx 1600$ kg/m^{2}s, inlet subcooling of $\Delta T_{sub,in} \approx 30$°C, and heat flux of $q''_w = 17.7$ W/cm^2 = 41.5% q''_{CHF} in microgravity. Time interval between successive images is 0.002 s.

(iii) Pressure fluctuations propagate upstream but are suppressed the further upstream the measurement is from the FBM. Compared to the FBM, the amplitude is slightly smaller at the BHM inlet, significantly smaller at the pump outlet, and negligible at the pump inlet.

(iv) Downstream of the FBM, pressure fluctuations are suppressed at the condenser outlet, which is the next available pressure measurement, and subcooled liquid exiting the condenser proceeds undisturbed to the pump inlet.

(v) The accumulator pressure is relatively steady, but this measurement is made on the airside.

While the effects of the instability are dispersed throughout the flow loop, the root cause is a local phenomenon and not instigated by interactions between different components at the system level. The rise in pressure at the upstream components is a symptom of the obstructed flow downstream of the heated length. The observed instability is better aligned with device-level DWOs, exhibiting several trends observed in the literature [35], including increasing q''_w destabilizing the flow, increasing G stabilizing the flow, and increasing $\Delta T_{sub,in}$ being either stabilizing or destabilizing. Additionally, the liquid backflow causing vapor to condense resembles the moving boiling boundary in conventional DWOs, which disrupts phase change and alters local density and velocity.

For comparable operating conditions, the frequency and amplitude of p_{in} fluctuations conditions deviated between μg_e and g_e. Not only were the p_{in} signals different, but the liquid backflow corresponding to severe p_{in} fluctuations in μg_e was absent in g_e. The instability source during vertical upflow boiling in g_e, resulting in atypical DWOs, is simply explained by the opposing forces of inertia and buoyancy, as detailed in [47]. The precise cause exacerbating instabilities in μg_e is less clear. Based on the observations in the present and previous sections, instability is likely instigated by non-equilibrium effects downstream of the heated length. Instabilities are most severe at high $\Delta T_{sub,in}$, and high q''_w, where non-equilibrium is most pronounced, but are suppressed at low $\Delta T_{sub,in}$, where the liquid and vapor are closer to equilibrium. Furthermore, pressure fluctuations observed within the FBM propagate to upstream components but are suppressed further downstream. The fluctuations are correlated to liquid backflow from the outlet of the channel as flow reverses downstream of the heated length. This suggests that the instability originates between the heated section outlet and the condenser. However, the lack of sufficient measurements and flow

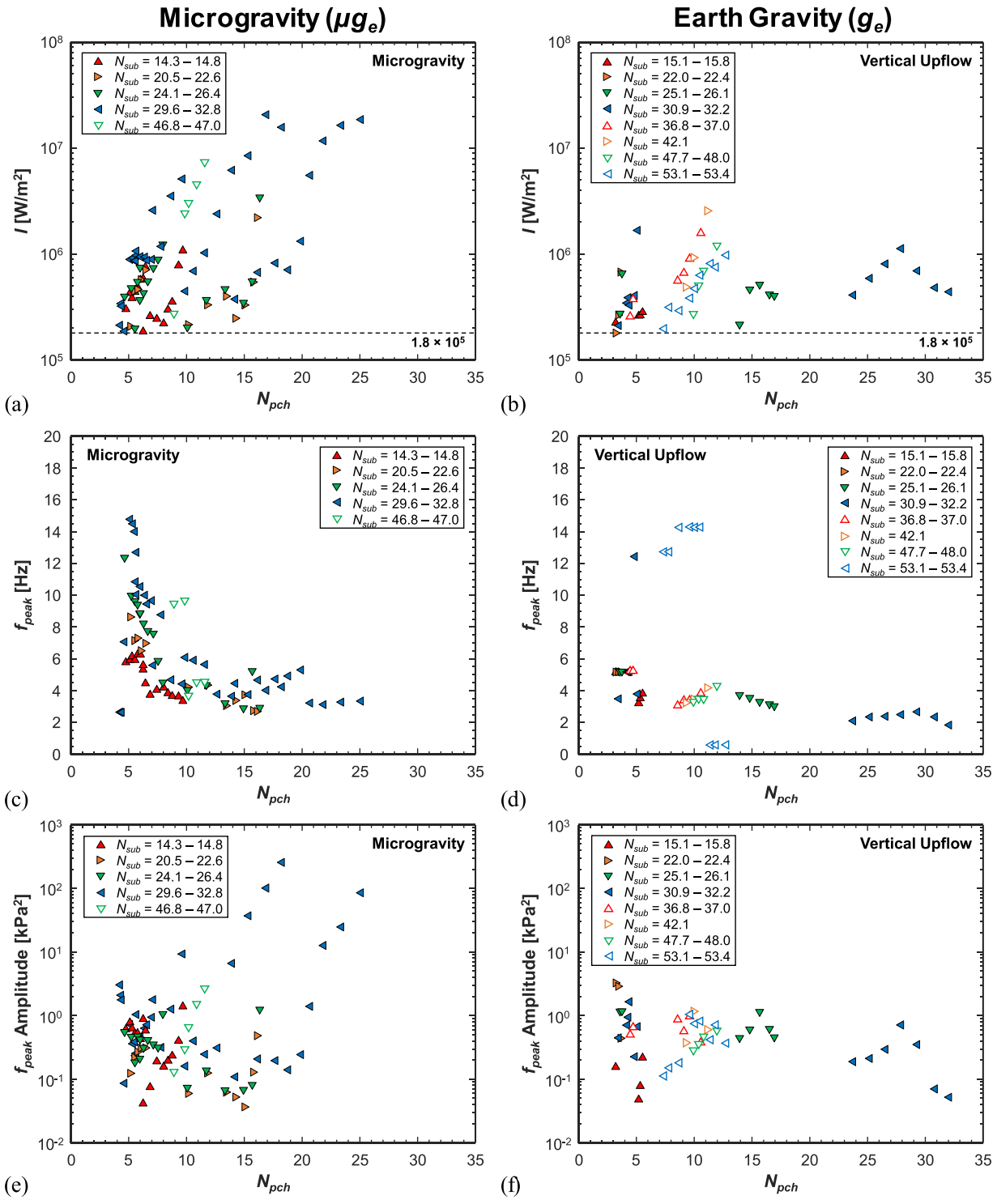

Fig. 15. Various terms characterizing p_{in} fluctuations plotted with respect to phase change number, N_{pch}, for different ranges of subcooling number, N_{sub}: pressure fluctuation intensity, I, in (a) μg_e and (b) g_e, power spectrum peak frequency, f_{peak}, in (c) μg_e and (d) g_e, and its corresponding amplitude in (e) μg_e and (f) g_e.

visualization immediately downstream of the FBM's heated length preclude confirmation of this hypothesis.

4.3. Assessment of Stability Criteria

Until this point, discussion was focused on physical observations and experimental trends of instability. However, *onset of flow instability* (OFI) is an important topic to distinguish between stable and unstable operating conditions. Stability maps are frequently used to visualize and differentiate between these conditions. Figs. 17 (a) and 17 (b) are plotted as $x_{e,out}$ versus Re_{fo}, as suggested by Brutin and Tadrist [60]. Their instability was identified by pressure fluctuations that occurred on the positive slope portion of the characteristic curve at low flow rates. The authors proposed a linear relation, with a slope dependent on inlet conditions, between $x_{e,out,OFI}$ and Re_{fo}. However, OFI criteria for the present database does not conform to this trend and a single line could not demarcate stable and unstable operating conditions in μg_e or g_e.

Bogojevic *et al.* [61] developed a stability map for flow boiling in a

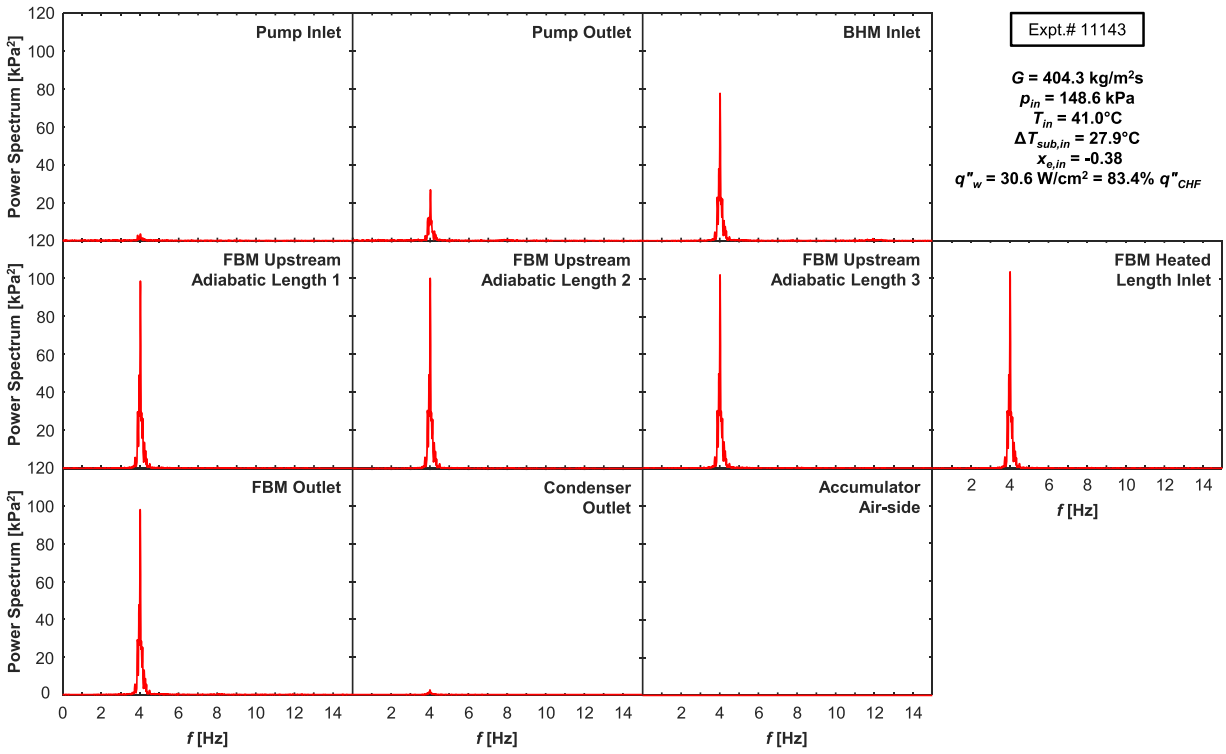

Fig. 16. Power spectrum by fast Fourier transform of pressure signals measured around the flow loop during the final 120 seconds of the heating increment during a mass velocity of $G \approx 400$ kg/m^{2}s, inlet subcooling of $\Delta T_{sub,in} \approx 30$°C, and heat flux of $q''_w = 30.6$ W/cm^2 = 83.4% q''_{CHF} in microgravity.

parallel micro-channel heat sink using G and q''_w. Two types of instabilities manifested as pressure and temperature oscillations, one with high amplitude and low frequency, and the other with low amplitude and high frequency. Linear criteria were derived to demarcate the map into stable flow ($q''_w/G < 0.99$ kJ/kg), instabilities with high amplitude and low frequency (0.99 kJ/kg $< q''_w/G <$ 1.55 kJ/kg), and instability with low amplitude and high frequency ($q''_w/G >$ 1.55 kJ/kg). However, this methodology is not effective for the present database in Figs. 17 (c) and 17 (d).

Several authors have utilized N_{pch} and N_{sub} to establish the stability boundaries of their systems [62–64]. The present data is plotted on these axes to create a similar stability map. A noticeable trend from the maps in Figs. 17 (e) and 17 (f) is that the flow is stable at $N_{sub} < 14$. However, a comprehensive OFI criterion cannot be determined from this plot due to the overlapping stable and unstable datapoints.

The two-dimensionality of stability maps constrains their use to narrow operating conditions. An alternative method of representing the OFI is through correlations, which can incorporate additional parameters. Of the 46 experimental cases conducted, 25 exhibited a transition from stable to unstable flow, allowing for the identification of OFI. The OFI point is determined as the average q''_w of the first heating increment displaying instability and the preceding stable increment, as the true OFI value will lie between these two values. The inlet conditions G, p_{in} and $\Delta T_{sub,in}$, corresponding to OFI are the average inlet conditions during each case. The OFI data is employed to evaluate correlations from the literature, presented in Table 2. Included with each correlation is its corresponding mean absolute error, MAE, defined as,

$$MAE(\%) = \frac{1}{N}\sum \left| \frac{OFI_{pred} - OFI_{\exp}}{OFI_{\exp}} \right| \times 100\%. \quad (12)$$

Kennedy *et al.* [65] relied on a simple relation estimating q''_{OFI} as 90% of the q''_w required to bring the fluid to saturation, $x_e = 0$. Their OFI point was identified as the local minimum on the internal characteristic curve, corresponding to the onset of either Ledinegg instability or PDO. However, their correlation did not accurately capture the current OFI data, resulting in a 370.1% MAE. Al-Yahia and Jo [39] proposed a similar correlation, but incorporated the channel's heated-to-wetted perimeter ratio and pressure, resulting in a lower MAE of 36.6%. The authors identified OFI through a sudden change in pressure drop accompanied by large p_{in} fluctuations. Lu *et al.* [40] determined their OFI by the onset of flow rate and temperature fluctuations. In some instances, these fluctuations were initiated by an excursion to a different flow rate, a symptom of Ledinegg Instability. The authors proposed a correlation that incorporated channel size by including Co as a multiplier. This form is not useful for the μg_e data, but the correlation predicts the vertical upflow OFI data with a 1011.4% MAE. Developed from water data with comparatively large N_{pch}, their correlation does not extrapolate well to the present database. Lim *et al.* [66] identified OFI by a rapid increase in the STD of p_{in}, which was attributed to rapid condensation of vapor by subcooled liquid. A parametric assessment of experimental parameters led to the development of a new correlation. Their correlation separated the influence of G and $\Delta T_{sub,in}$ by including both Ja^{**} and Re_{fo}, resulting in an 18.8% MAE.

A new correlation for the $x_{e,out}$ corresponding to OFI is developed using the 25 OFI data points. Observations from section 3 indicate OFI primarily depends on G and $\Delta T_{sub,in}$, which are non-dimensionalized as Re_{fo} and $x_{e,in}$. Bond number, Bd, accounts for the influence of gravity in a manner that is functional in both μg_e and g_e. Nonlinear regression is performed on a simple functional form in MATLAB [58], resulting in

$$\left(1 + x_{e,out,OFI}\right) = 1.643\left(1 + x_{e,in}\right)^{0.776} \mathrm{Re}_{fo}^{-0.054} \left(1 + Bd\right)^{0.012}. \quad (13)$$

The ranges of OFI data used to develop the correlation are Re_{fo} = 1795.4 – 28780.9, $x_{e,in}$ = -0.63 – -0.19, Bd = 0.0 – 23.2, and $x_{e,out}$ = -0.54 – -0.10. A parity plot of the predicted $x_{e,out,OFI}$ in μg_e and g_e is shown in Fig. 18 (a). The new correlation predicts the OFI data with a superior MAE of 1.3%, and 96% of the database is predicted within 10% of experimental values. Figs. 18 (b) and 18 (c) demonstrate predicted trends of the new correlation with respect to Re_{fo} and $x_{e,in}$, respectively, compared to experimental data. In Fig. 18 (b), the correlation captures the trend of decreasing $x_{e,out,OFI}$ with increasing Re_{fo}, for a fixed $x_{e,in}$. The

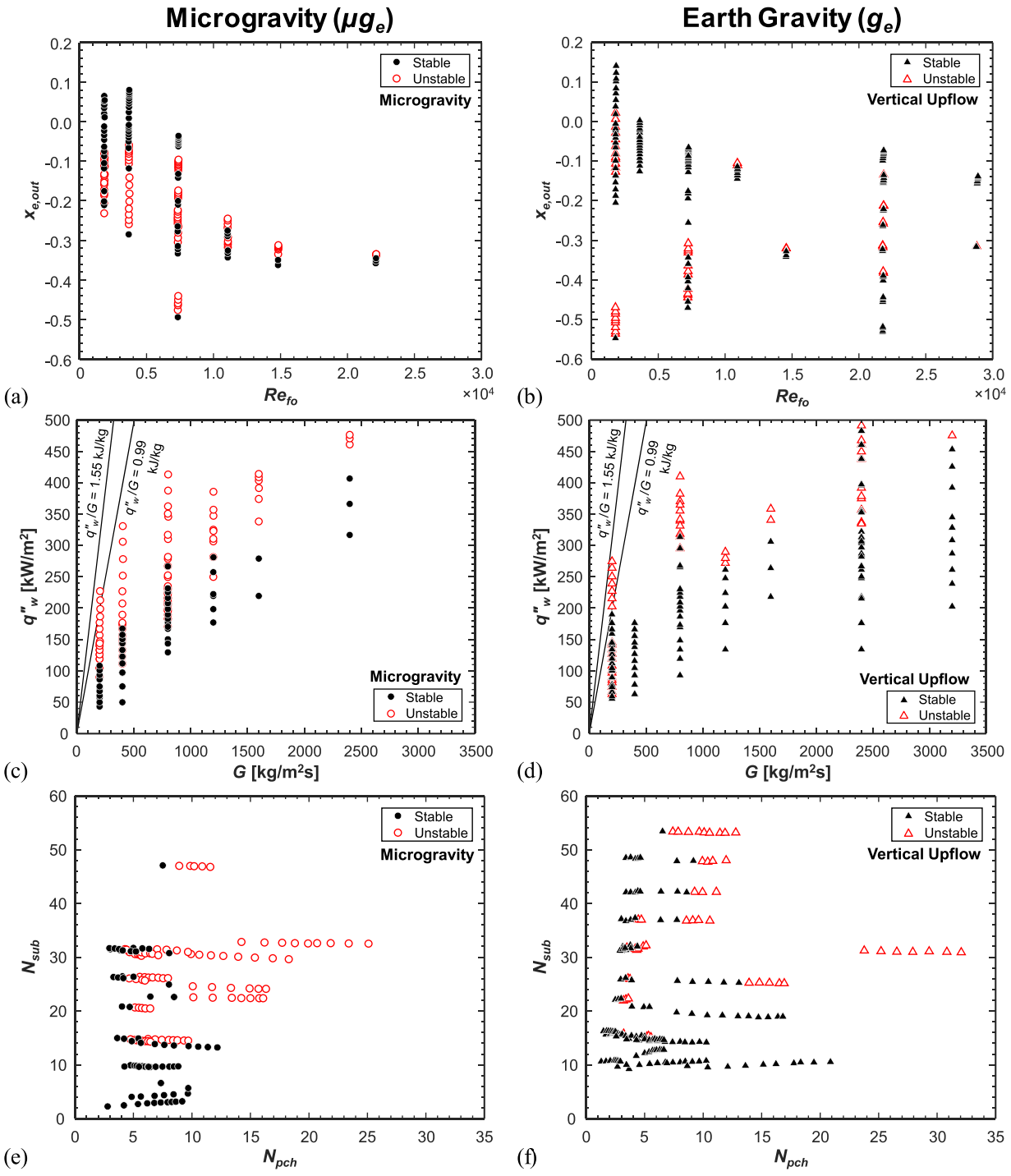

Fig. 17. Assessment of various proposed stability maps including Re_{fo} and $x_{e,out}$ [60] for the (a) μg_e and (b) g_e data, G and q''_w [61] for the (c) μg_e and (d) g_e data, and N_{pch} and N_{sub} [62-64] for the (e) μg_e and (f) g_e data.

correlation correctly predicts the data at low Re_{fo} as unstable, even though no OFI points are present. The predicted $x_{e,out,OFI}$ is also consistently lower in μg_e, where the flow is more susceptible to instabilities. Fig. 18 (c) shows the new correlation accurately captures $x_{e,out,OFI}$ increasing with increasing $x_{e,in}$ and the boundary between stable and unstable conditions. As observed in the stability maps in Figs. 17 (e) and 17 (f), instabilities are not observed for $N_{sub} < 14$. Therefore, OFI predictions of the correlation are limited to $x_{e,in} < -0.18$.

In closing, the investigation of flow boiling instabilities presented in this study provides a foundation to develop predictive methods for various aspects of two-phase flow, coinciding with the ambition of the Purdue University Boiling and Two-Phase Flow Laboratory since the 1980s. In addition to empirical correlations such as that presented in Eq. (13), methodologies for computational tools, including machine learning algorithms [32,67–69] and computational fluid dynamics [70, 71], have been previously presented and are capable of capturing complex two-phase flow physics.

5. Conclusions

This study elaborated on instabilities observed during the Flow Boiling and Condensation Experiment's microgravity flow boiling

Table 2
OFI correlations available in the literature.

Authors	Correlation	MAE
Kennedy *et al.* (2000) [65]	$q''_{OFI} = 0.9\frac{GA_c c_{p,f}\Delta T_{sub,in}}{P_h L_h}$	370.1%
Al-Yahia and Jo (2018) [39]	$q''_{OFI} = 0.8\frac{GA_c c_{p,f}\Delta T_{sub,in}}{P_h L_h}\frac{P_h}{P_w}\left(\frac{p_{in}}{1.12\times10^5}\right)^{0.4}$	36.6%
Lu *et al.* (2019) [40]	$N_{pch,OFI} = Co^{-0.24}\left(4.84N_{sub}^{0.60} + 1.98We_{fo}^{-0.84}\left(\frac{\rho_f}{\rho_g}\right)^{0.64}\right)$	1011.4%
Lim *et al.* (2021) [66]	$q''_{OFI} = 3.034Ja**^{-0.7612}\left(\frac{p_{in}}{1.12\times10^5}\right)^{-0.02467}\mathrm{Re}_{fo}^{-0.375}\frac{GA_c c_{p,f}\Delta T_{sub,in}}{P_h L_h}$	18.8%

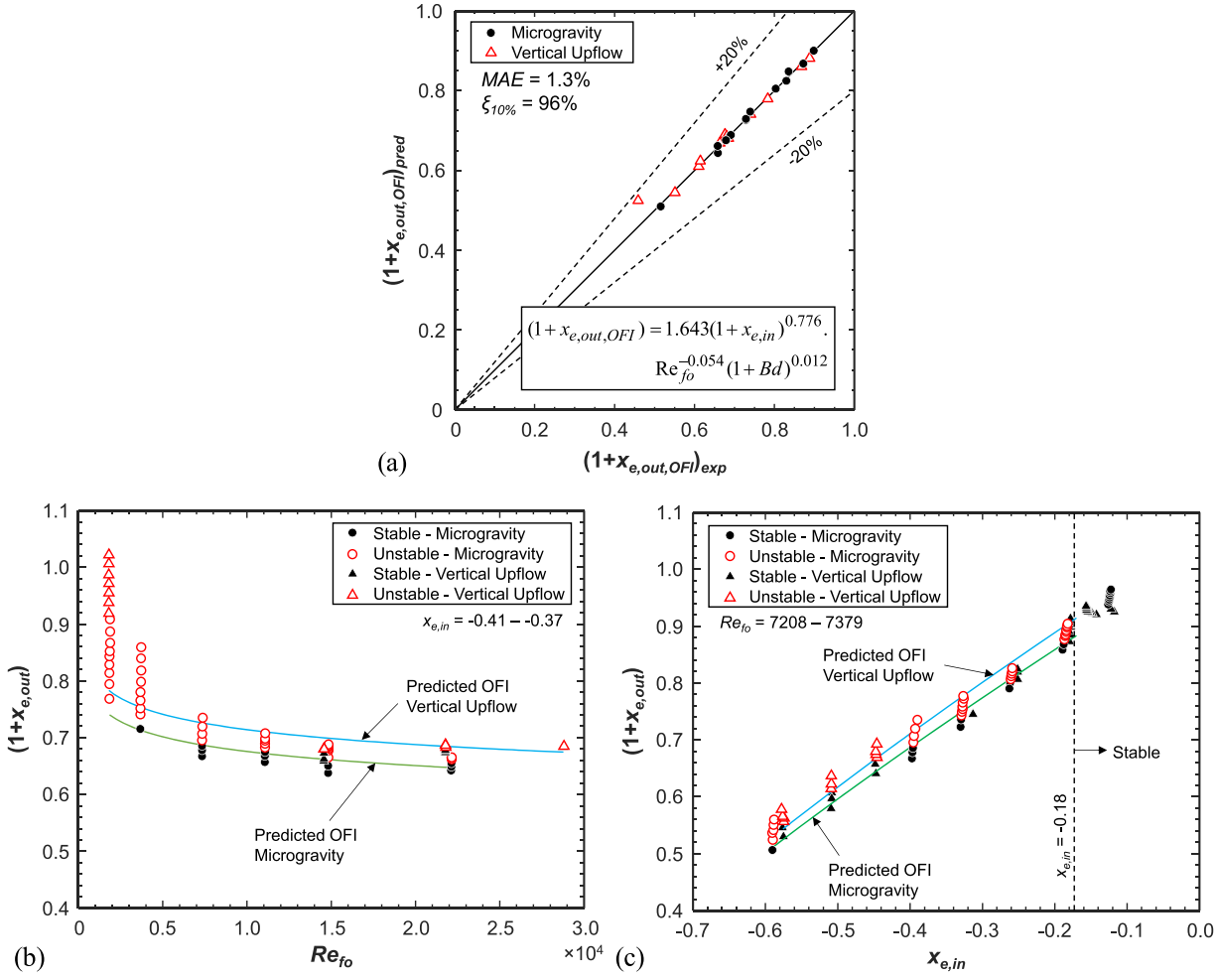

Fig. 18. (a) Parity plot of the new OFI correlation and comparisons of experimental results to predicted parametric trends with respect to (b) Re_{fo} and (c) $x_{e,in}$ in both μg_e and g_e.

experiments onboard the ISS [25–27]. Experiments were performed with enhanced data sampling frequency and extended image recording duration to further investigate the instability. Data was gathered in microgravity and Earth gravity during vertical upflow. Key conclusions are as follows:

(1) Meticulous observation of flow visualization identified instabilities manifesting as cyclic disruptions of flow. The frequency of the instability observed within the channel was correlated to that of p_{in} oscillations, via Fourier analysis. The instability was not correlated to variations in Dp or $\dot{m}$ and exhibited behavior similar to density wave oscillations. However, p_{in} variations alone were not indicative of instability. Instabilities were observed when the pseudo-intensity of the p_{in} fluctuations, I, exceeded 1.8×10^5 W/m^2.

(2) Instabilities were exacerbated at low flow rates, high inlet subcoolings, and high heat fluxes. At their most severe, instabilities manifested as liquid backflow from the outlet that penetrated through the channel, condensing vapor in its wake. This resulted in a power spectrum peak frequency (f_{peak}) amplitude of up to 256.9 kPa^2. Instabilities during vertical upflow in Earth gravity were comparatively mild with a maximum f_{peak} amplitude of 3.3 kPa^2 and flow reversal never occurred.

(3) Various methods to predict the system's stability were assessed. Two-dimensional stability maps were unable to capture the complex dependency of system stability on numerous parameters. However, the stability maps showed instabilities are

effectively suppressed for $N_{sub} < 14$. The best performing correlation available in the literature to predict the Onset of Flow Instability (OFI) was that by Lim *et al.* [66], which predicted the OFI subset of the database with an 18.8% MAE.

(4) A new simple correlation was developed that differentiates between microgravity and Earth gravity and predicts the OFI data with a 1.3% MAE. Not only does the new correlation predict the present data with superior accuracy but it also captures parametric trends of OFI and correctly categorizes data where OFI was not captured.

CRediT authorship contribution statement

Issam Mudawar: Writing – review & editing, Visualization, Validation, Supervision, Resources, Project administration, Methodology, Investigation, Funding acquisition, Formal analysis, Data curation, Conceptualization. **Steven J. Darges:** Writing – review & editing, Writing – original draft, Visualization, Validation, Software, Methodology, Investigation, Formal analysis, Data curation, Conceptualization. **V.S. Devahdhanush:** Writing – review & editing, Writing – original draft, Validation, Investigation, Data curation. **Mohammad M. Hasan:** Writing – review & editing, Supervision, Resources, Project administration, Funding acquisition, Data curation. **Henry K. Nahra:** Writing – review & editing, Supervision, Resources, Project administration, Funding acquisition, Data curation. **R. Balasubramaniam:** Writing – review & editing, Supervision, Data curation. **Jeffrey R. Mackey:** Writing – review & editing, Visualization, Methodology, Data curation.

Declaration of competing interest

The authors declare the following financial interests/personal relationships which may be considered as potential competing interests:

Issam Mudawar reports financial support was provided by NASA. If there are other authors, they declare that they have no known competing financial interests or personal relationships that could have appeared to influence the work reported in this paper.

Data availability

The experimental raw data used in this paper will be publicly made available in a NASA repository later.

Acknowledgement

The authors acknowledge the support of the National Aeronautics and Space Administration (NASA) under grant no. 80NSSC22K0328. The authors thank the FBCE team at NASA Glenn Research Center, Cleveland, Ohio, especially Nancy Hall (FBCE Project Manager), Rochelle May, Jose Lombay-Gonzales, and Phillip Gonia (Software Engineering), Mark Sorrells (Assembly, Integration and Test Lead), Jesse deFiebre (Fluids Lead), Monica Guzik (FBCE Chief Engineer), and ZIN FCF Mission Operations Team, for their dedicated technical assistance and successful completion of ISS testing of FBCE's FBM.

Appendix A. ISS Experiment Summary

Summaries of instability experiments are provided in Tables A.1 and A.2 for experiments performed in microgravity and Earth gravity during vertical upflow, respectively. To cross-reference the data reported in this study to the original database (which will be made available to the community via a NASA repository later), experiment reference numbers (Expt.#) are provided for each set of operating conditions, along with average values of mass velocity, G, inlet pressure, p_{in}, and inlet subcooling, $\Delta T_{sub,in}$ during each case. The naming convention for Expt.# is the latter four digits of the five-digit number represent unique case numbers while the first digit represents the trial number. For example, Expt.# 11118 denotes the first trial of case 1118.

Table A.1
Summary of flow boiling instability experiments performed onboard the ISS in microgravity. The included values represent average steady state conditions during each run.

Experiment Reference Number (Expt.#)	G [kg/m^{2}s]	p_{in} [kPa]	$\Delta T_{sub,in}$ [°C]
11118	200.0	147.5	4.0
11119	400.0	150.0	2.6
11131	399.9	148.5	13.7
11132	800.1	148.8	13.7
11142	201.6	146.9	30.4
11143	401.6	148.0	28.4
11144	800.5	147.3	29.4
11145	1599.9	151.0	29.6
11146	2400.1	149.0	29.9
11231	200.6	147.6	22.9
11232	200.2	146.9	20.8
11233	200.0	152.0	6.7
11237	800.5	147.3	44.2
11240	800.2	146.6	24.3
11241	800.2	148.1	19.2
11242	800.0	149.1	9.2
11279	1200.0	149.3	29.3
11279*	399.9	147.4	8.9
11281	1200.0	148.8	24.5
21130	200.0	146.9	12.8

*Case 11279 was repeated under the same name; this denotes the experiment performed on July 26, 2023.

Table A.2
Summary of flow boiling instability experiments performed in terrestrial gravity during vertical upflow. The included values represent average steady state conditions during each run.

Experiment Reference Number (Expt.#)	G [kg/m^{2}s]	p_{in} [kPa]	$\Delta T_{sub,in}$ [°C]
11119	399.9	141.8	8.9
11130	200.0	139.9	48.2
11131	399.9	142.2	12.9
11134	2400.0	144.6	14.4
11135	3200.0	141.5	14.4
11142	199.9	141.3	28.0
11145	1599.9	144.6	29.4
11146	2400.0	143.4	28.6
11147	3199.9	140.3	28.0
11231	199.9	141.7	22.8
11232*	199.9	142.7	17.3
11233	199.7	146.2	9.3
11237	800.0	141.2	43.4
11238	800.1	141.8	38.2
11239	800.1	142.4	33.4
11240	800.0	142.8	23.3
11241	800.0	142.2	18.6
11242	800.0	143.6	10.6
11246	2400.0	143.3	44.6
11247	2400.0	143.6	38.6
11248	2400.0	144.0	33.9
11249	2400.0	143.8	23.8
11250	2400.0	144.3	20.2
11251	2400.0	144.3	9.6
11280	1200.0	144.4	13.9
21132	800.0	143.1	13.2

*Case 11232 was repeated under the same name; this denotes the experiment performed on July 31, 2023.

References

[1] I. Mudawar, Two-phase microchannel heat sinks: theory, applications, and limitations, J. Electron. Packag. 133 (4) (2011) 041002, https://doi.org/10.1115/1.4005300.

[2] F.P. Chiaramonte, J. McQuillen, H.K. Nahra, P. Manoharan, H. Vanhala, B.J. Motil, J. Kim, V. Carey, W.G. Anderson, J. Plawsky, L. Carter, A. Jackson, NASA Division of Space and Life and Phyiscal Sciences Research and Applications Fluid Physics Workshop Report, Cleveland, OH, USA, 2019, 2020.

[3] T.J. LaClair, I. Mudawar, Thermal transients in a capillary evaporator prior to the initiation of boiling, Int. J. Heat Mass Transfer 43 (21) (2000) 3937–3952, https://doi.org/10.1016/S0017-9310(00)00042-9.

[4] G. Liang, I. Mudawar, Pool boiling critical heat flux (CHF) – Part 2: Assessment of models and correlations, Int. J. Heat Mass Transfer 117 (2018) 1368–1383, https://doi.org/10.1016/j.ijheatmasstransfer.2017.09.073.

[5] I. Mudawar, R.A. Houpt, Mass and momentum transport in smooth falling liquid films laminarized at relatively high Reynolds numbers, Int. J. Heat Mass Transfer 36 (14) (1993) 3437–3448, https://doi.org/10.1016/0017-9310(93)90162-Y.

[6] I. Mudawar, D.E. Maddox, Enhancement of critical heat flux from high power microelectronic heat sources in a flow channel, J. Electron. Packag. 112 (3) (1990) 241–248, https://doi.org/10.1115/1.2904373.

[7] C.O. Gersey, I. Mudawar, Effects of heater length and orientation on the trigger mechanism for near-saturated flow boiling critical heat flux—II. Critical heat flux model, Int. J. Heat Mass Transfer 38 (4) (1995) 643–654, https://doi.org/10.1016/0017-9310(94)00194-Z.

[8] S. Mukherjee, I. Mudawar, Pumpless loop for narrow channel and micro-channel boiling, J. Electron. Packag. 125 (3) (2003) 431–441, https://doi.org/10.1115/1.1602708.

[9] M.E. Johns, I. Mudawar, An ultra-high power two-phase jet-impingement avionic clamshell module, J. Electron. Packag. 118 (4) (1996) 264–270, https://doi.org/10.1115/1.2792162.

[10] W.P. Klinzing, J.C. Rozzi, I. Mudawar, Film and transition boiling correlations for quenching of hot surfaces with water sprays, J. Heat Treat. 9 (2) (1992) 91–103, https://doi.org/10.1007/BF02833145.

[11] M.K. Sung, I. Mudawar, Single-phase and two-phase heat transfer characteristics of low temperature hybrid micro-channel/micro-jet impingement cooling module, Int. J. Heat Mass Transfer 51 (15–16) (2008) 3882–3895, https://doi.org/10.1016/j.ijheatmasstransfer.2007.12.016.

[12] M.K. Sung, I. Mudawar, Single-phase and two-phase hybrid cooling schemes for high-heat-flux thermal management of defense electronics, J. Electron. Packag. 131 (2) (2009) 021013, https://doi.org/10.1115/1.3111253.

[13] Y. Ma, J.N. Chung, An experimental study of critical heat flux (CHF) in microgravity forced-convection boiling, Int. J. Multiphase Flow 27 (10) (2001) 1753–1767, https://doi.org/10.1016/S0301-9322(01)00031-3.

[14] B. Liu, B. Yuan, P. Xu, J. Zhao, Y. Zhang, J. Wei, Y. Yang, Q. Cao, A method for approximating the CHF of subcooled flow boiling in microgravity by ground tests, Int. J. Multiphase Flow 122 (2020) 103161, https://doi.org/10.1016/j.ijmultiphaseflow.2019.103161.

[15] M. Narcy, E. de Malmazet, C. Colin, Flow boiling in tube under normal gravity and microgravity conditions, Int. J. Multiphase Flow 60 (2014) 50–63, https://doi.org/10.1016/j.ijmultiphaseflow.2013.11.011.

[16] M.T. Lebon, C.F. Hammer, J. Kim, Gravity effects on subcooled flow boiling heat transfer, Int. J. Heat Mass Transfer 128 (2019) 700–714, https://doi.org/10.1016/j.ijheatmasstransfer.2018.09.011.

[17] D.M. Iceri, G. Zummo, L. Saraceno, G. Ribatski, Convective boiling heat transfer under microgravity and hypergravity conditions, Int. J. Heat Mass Transfer 153 (2020) 119614, https://doi.org/10.1016/j.ijheatmasstransfer.2020.119614.

[18] C. Konishi, I. Mudawar, Review of flow boiling and critical heat flux in microgravity, Int. J. Heat Mass Transfer 80 (2015) 469–493, https://doi.org/10.1016/j.ijheatmasstransfer.2014.09.017.

[19] P. Di Marco, W. Grassi, Pool boiling in microgravity: Assessed results and open issues, in: Proc. 3rd European Therm. Conf, Heidelberg, Germany, 2000, pp. 81–90.

[20] N.J. Penley, C.P. Schafer, J.D.F. Bartoe, The international space station as a microgravity research platform, Acta Astronaut 50 (11) (2002) 691–696, https://doi.org/10.1016/S0094-5765(02)00003-6.

[21] K. Inoue, H. Ohta, Y. Toyoshima, H. Asano, O. Kawanami, R. Imai, K. Suzuki, Y. Shinmoto, S. Matsumoto, Heat loss analysis of flow boiling experiments onboard international space station with unclear thermal environmental conditions (1st report: subcooled liquid flow conditions at test section inlet), Microgravity Sci. Tec. 33 (2) (2021) 28, https://doi.org/10.1007/s12217-021-09869-5.

[22] K. Inoue, H. Ohta, H. Asano, O. Kawanami, R. Imai, K. Suzuki, Y. Shinmoto, T. Kurimoto, S. Matsumoto, Heat loss analysis of flow boiling experiments onboard international space station with unclear thermal environmental conditions (2nd report: liquid-vapor two-phase flow conditions at test section inlet), Microgravity Sci. Tec. 33 (5) (2021) 57, https://doi.org/10.1007/s12217-021-09902-7.

[23] V.S. Devahdhanush, I. Mudawar, H.K. Nahra, R. Balasubramaniam, M.M. Hasan, J. R. Mackey, Experimental heat transfer results and flow visualization of vertical upflow boiling in Earth gravity with subcooled inlet conditions – In preparation for experiments onboard the International Space Station, Int. J. Heat Mass Transfer 188 (2022) 122603, https://doi.org/10.1016/j.ijheatmasstransfer.2022.122603.

[24] V.S. Devahdhanush, S.J. Darges, I. Mudawar, H.K. Nahra, R. Balasubramaniam, M. M. Hasan, J.R. Mackey, Flow visualization, heat transfer, and critical heat flux of flow boiling in Earth gravity with saturated liquid-vapor mixture inlet conditions – In preparation for experiments onboard the International Space Station, Int. J. Heat Mass Transfer 192 (2022) 122890, https://doi.org/10.1016/j.ijheatmasstransfer.2022.122890.

[25] I. Mudawar, V.S. Devahdhanush, S.J. Darges, M.M. Hasan, H.K. Nahra, R. Balasubramaniam, J.R. Mackey, Heat transfer and interfacial flow physics of microgravity flow boiling in single-side-heated rectangular channel with subcooled inlet conditions – Experiments onboard the International Space Station, Int. J. Heat

Mass Transfer 207 (2023) 123998, https://doi.org/10.1016/j.ijheatmasstransfer.2023.123998.
[26] I. Mudawar, V.S. Devahdhanush, S.J. Darges, M.M. Hasan, H.K. Nahra, R. Balasubramaniam, J.R. Mackey, Effects of heating configuration and operating parameters on heat transfer and interfacial physics of microgravity flow boiling with subcooled inlet conditions – Experiments onboard the International Space Station, Int. J. Heat Mass Transfer 217 (2023) 124732, https://doi.org/10.1016/j.ijheatmasstransfer.2023.124732.
[27] I. Mudawar, V.S. Devahdhanush, S.J. Darges, M.M. Hasan, H.K. Nahra, R. Balasubramaniam, J.R. Mackey, Microgravity flow boiling experiments with liquid-vapor mixture inlet onboard the International Space Station, Int. J. Heat Mass Transfer 224 (2024) 125299, https://doi.org/10.1016/j.ijheatmasstransfer.2024.125299.
[28] I. Mudawar, S.J. Darges, V.S. Devahdhanush, Parametric experimental trends, interfacial behavior, correlation assessment, and interfacial lift-off model predictions of critical heat flux for microgravity flow boiling with subcooled inlet conditions – Experiments onboard the International Space Stat, Int. J. Heat Mass Transfer 213 (2023) 124296, https://doi.org/10.1016/j.ijheatmasstransfer.2023.124296.
[29] I. Mudawar, S.J. Darges, V.S. Devahdhanush, Critical heat flux for flow boiling with saturated two-phase inlet in microgravity onboard the International Space Station, Int. J. Heat Mass Transfer 233 (2024) 126017, https://doi.org/10.1016/j.ijheatmasstransfer.2024.126017.
[30] V.S. Devahdhanush, I. Mudawar, Subcooled flow boiling heat transfer in a partially-heated rectangular channel at different orientations in Earth gravity, Int. J. Heat Mass Transfer 195 (2022) 123200, https://doi.org/10.1016/j.ijheatmasstransfer.2022.123200.
[31] S.J. Darges, V.S. Devahdhanush, I. Mudawar, Assessment and development of flow boiling critical heat flux correlations for partially heated rectangular channels in different gravitational environments, Int. J. Heat Mass Transfer 196 (2022) 123291, https://doi.org/10.1016/j.ijheatmasstransfer.2022.123291.
[32] I. Mudawar, S.J. Darges, V.S. Devahdhanush, Prediction technique for flow boiling heat transfer and critical heat flux in both microgravity and Earth gravity via artificial neural networks (ANNs), Int. J. Heat Mass Transfer 220 (2024) 124998, https://doi.org/10.1016/j.ijheatmasstransfer.2023.124998.
[33] J.A. Boure, A.E. Bergles, L.S. Tong, Review of two-phase flow instability, Nucl. Eng. Des. 25 (2) (1973) 165–192, https://doi.org/10.1016/0029-5493(73)90043-5.
[34] R.T. Lahey Jr., M.Z. Podowski, On the analysis of various instabilities in two-phase flows, Multiphase Science and Technology 4 (1–4) (1989) 183–370, https://doi.org/10.1615/MultScienTechn.v4.i1-4.30.
[35] L.E. O'Neill, I. Mudawar, Review of two-phase flow instabilities in macro- and micro-channel systems, Int. J. Heat Mass Transfer 157 (2020) 119738, https://doi.org/10.1016/j.ijheatmasstransfer.2020.119738.
[36] C. Li, X. Fang, Q. Dai, Two-phase flow boiling instabilities: A review, Annals of Nuclear Energy 173 (2022) 109099, https://doi.org/10.1016/j.anucene.2022.109099.
[37] Z. Ma, X. Fang, An overview of gravity effects on flow boiling instabilities, Progress in Aerospace Sciences 128 (2022) 100764, https://doi.org/10.1016/j.paerosci.2021.100764.
[38] R.H. Whittle, R. Forgan, A correlation for the minima in the pressure drop versus flow-rate curves for sub-cooled water flowing in narrow heated channels, Nucl. Eng. Des. 6 (1) (1967) 89–99, https://doi.org/10.1016/0029-5493(67)90049-0.
[39] O.S. Al-Yahia, D. Jo, ONB, OSV, and OFI for subcooled flow boiling through a narrow rectangular channel heated on one-side, Int. J. Heat Mass Transfer 116 (2018) 136–151, https://doi.org/10.1016/j.ijheatmasstransfer.2017.09.011.
[40] Q. Lu, Y. Zhang, Y. Liu, L. Zhou, C. Shen, D. Chen, An experimental investigation on the characteristics of flow instability with the evolution of two-phase interface morphology, Int. J. Heat Mass Transfer 138 (2019) 468–482, https://doi.org/10.1016/j.ijheatmasstransfer.2019.04.082.
[41] R.D. Boyd, Subcooled flow boiling critical heat flux (CHF) and its application to fusion energy components. part I. A review of fundamentals of CHF and related data base, Fusion Technol 7 (1) (1985) 7–30, https://doi.org/10.13182/FST85-A24515.
[42] T.J. Heindel, S. Ramadhyani, F.P. Incropera, Liquid immersion cooling of a longitudinal array of discrete heat sources in protruding substrates: II—Forced convection boiling, J. Electron. Packag. 114 (1) (1992) 63–70, https://doi.org/10.1115/1.2905443.
[43] J.L. Plawsky, P.C. Wayner, Explosive nucleation in microgravity: The constrained vapor bubble experiment, Int. J. Heat Mass Transfer 55 (23–24) (2012) 6473–6484, https://doi.org/10.1016/j.ijheatmasstransfer.2012.06.047.
[44] A.K. Nayak, P.K. Vijayan, V. Jain, D. Saha, R.K. Sinha, Study on the flow-pattern-transition instability in a natural circulation heavy water moderated boiling light water cooled reactor, Nucl. Eng. Des. 225 (2–3) (2003) 159–172, https://doi.org/10.1016/S0029-5493(03)00153-5.
[45] K. Fukuda, T. Kobori, Classification of two-phase flow instability by density wave oscillation model, J. Nucl. Sci. Tec. 16 (2) (1979) 95–108.
[46] R. Khodabandeh, R. Furberg, Instability, heat transfer and flow regime in a two-phase flow thermosyphon loop at different diameter evaporator channel, Appl. Therm. Eng. 30 (10) (2010) 1107–1114, https://doi.org/10.1016/j.applthermaleng.2010.01.024.
[47] L.E. O'Neill, I. Mudawar, M.M. Hasan, H.K. Nahra, R. Balasubramaniam, J. R. Mackey, Experimental investigation of frequency and amplitude of density wave oscillations in vertical upflow boiling, Int. J. Heat Mass Transfer 125 (2018) 1240–1263, https://doi.org/10.1016/j.ijheatmasstransfer.2018.04.138.
[48] S. Hayama, A study on the hydrodynamic instability in boiling channels : 3rd report, the modes of vibration in multi-channel system and the reverse flow, Bull. JSME 10 (38) (1967) 308–319, https://doi.org/10.1299/jsme1958.10.308.
[49] M.E. Rahman, S. Singh, Flow excursions and pressure drop oscillations in boiling two-phase channel, Int. J. Heat Mass Transfer 138 (2019) 647–658, https://doi.org/10.1016/j.ijheatmasstransfer.2019.04.025.
[50] S.S. Papell, An Instability Effect on Two-Phase Heat Transfer for Subcooled Water Flowing under Conditions of Zero Gravity, NASA Tech Note TN D-2259, 1964.
[51] W.R. Schlichting, An analysis of the effect of gravity on interacting DWO/PDO instability modes, Rensselaer Polytechnic Institute, 2009. Ph.D. thesis.
[52] H. He, P. Li, R. Yan, L. Pan, Modeling of reversal flow and pressure fluctuation in rectangular microchannel, Int. J. Heat Mass Transfer 102 (2016) 1024–1033, https://doi.org/10.1016/j.ijheatmasstransfer.2016.06.102.
[53] C. Baltis, G.P. Celata, M. Cumo, L. Saraceno, G. Zummo, Gravity influence on heat transfer rate in flow boiling, Microgravity Sci. Tec. 24 (3) (2012) 203–213, https://doi.org/10.1007/s12217-012-9298-5.
[54] W.A. Arnold, T.G. Hartman, J. McQuillen, Chemical characterization and thermal stressing studies of perfluorohexane fluids for space-based applications, J. Spacecraft Rockets 44 (1) (2007) 94–102, https://doi.org/10.2514/1.22537.
[55] H. Zhang, I. Mudawar, M.M. Hasan, Flow boiling CHF in microgravity, Int. J. Heat Mass Transfer 48 (15) (2005) 3107–3118, https://doi.org/10.1016/j.ijheatmasstransfer.2005.02.015.
[56] E.W. Lemmon, I.H. Bell, M.L. Huber, M.O. McLinden, NIST Standard Reference Database 23: Reference Fluid Thermodynamic and Transport Properties-REFPROP, Version 10, NIST, Gaithersburg, MD, USA, 2018.
[57] T. Zhang, Y. Peles, J.T. Wen, T. Tong, J.-Y. Chang, R. Prasher, M.K. Jensen, Analysis and active control of pressure-drop flow instabilities in boiling microchannel systems, Int. J. Heat Mass Transfer 53 (11–12) (2010) 2347–2360, https://doi.org/10.1016/j.ijheatmasstransfer.2010.02.005.
[58] MATLAB version: 9.13 (R2022b), The MathWorks Inc, 2022. https://www.mathworks.com.
[59] L.L. Beranek, T.J. Mellow, Acoustics: Sound Fields and Transducers. Acoustics: Sound Fields and Transducers, First, Elsevier, Oxford, UK, 2012, pp. 1–19, https://doi.org/10.1016/B978-0-12-391421-7.00001-4.
[60] D. Brutin, L. Tadrist, Pressure drop and heat transfer analysis of flow boiling in a minichannel: influence of the inlet condition on two-phase flow stability, Int. J. Heat Mass Transfer 47 (10–11) (2004) 2365–2377, https://doi.org/10.1016/j.ijheatmasstransfer.2003.11.007.
[61] D. Bogojevic, K. Sefiane, A.J. Walton, H. Lin, G. Cummins, Two-phase flow instabilities in a silicon microchannels heat sink, Int. J. Fluid Fl. 30 (5) (2009) 854–867, https://doi.org/10.1016/j.ijheatfluidflow.2009.03.013.
[62] M. Ishii, Study on Flow Instabilities in Two-Phase Mixtures (1976), https://doi.org/10.2172/7277361.
[63] K.H. Chang, C. Pan, Two-phase flow instability for boiling in a microchannel heat sink, Int. J. Heat Mass Transfer 50 (11–12) (2007) 2078–2088, https://doi.org/10.1016/j.ijheatmasstransfer.2006.11.014.
[64] L.E. O'Neill, I. Mudawar, M.M. Hasan, H.K. Nahra, R. Balasubramaniam, N.R. Hall, A. Lokey, J.R. Mackey, Experimental investigation into the impact of density wave oscillations on flow boiling system dynamic behavior and stability, Int. J. Heat Mass Transfer 120 (2018) 144–166, https://doi.org/10.1016/j.ijheatmasstransfer.2017.12.011.
[65] J.E. Kennedy, G.M. Roach, M.F. Dowling, S.I. Abdel-Khalik, S.M. Ghiaasiaan, S. M. Jeter, Z.H. Quershi, The onset of flow instability in uniformly heated horizontal microchannels, J. Heat Transfer 122 (1) (2000) 118–125, https://doi.org/10.1115/1.521442.
[66] J.H. Lim, S.W. Lee, M. Park, H. Oh, D. Hwang, M.H. Kim, H. Jo, New correlation to predict the onset of flow instability (OFI) heat flux of one-side heated hypervapotron channel for fusion reactor application, Physica Scripta 96 (12) (2021) 125614, https://doi.org/10.1088/1402-4896/ac25a4.
[67] Y. Qiu, D. Garg, L. Zhou, C.R. Kharangate, S.-M. Kim, I. Mudawar, An artificial neural network model to predict mini/micro-channels saturated flow boiling heat transfer coefficient based on universal consolidated data, Int. J. Heat Mass Transfer 149 (2020) 119211, https://doi.org/10.1016/j.ijheatmasstransfer.2019.119211.
[68] L. Zhou, D. Garg, Y. Qiu, S.M. Kim, I. Mudawar, C.R. Kharangate, Machine learning algorithms to predict flow condensation heat transfer coefficient in mini/micro-channel utilizing universal data, Int. J. Heat Mass Transfer 162 (2020) 120351, https://doi.org/10.1016/j.ijheatmasstransfer.2020.120351.
[69] Y. Qiu, D. Garg, S.M. Kim, I. Mudawar, C.R. Kharangate, Machine learning algorithms to predict flow boiling pressure drop in mini/micro-channels based on universal consolidated data, Int. J. Heat Mass Transfer 178 (2021) 121607, https://doi.org/10.1016/j.ijheatmasstransfer.2021.121607.
[70] I. Mudawar, J. Lee, Experimental and computational investigation into hydrodynamic and heat transfer characteristics of subcooled flow boiling on the International Space Station, Int. J. Heat Mass Transfer 207 (2023) 124000, https://doi.org/10.1016/j.ijheatmasstransfer.2023.124000.
[71] I. Mudawar, S. Kim, J. Lee, A coupled level-set and volume-of-fluid (CLSVOF) method for prediction of microgravity flow boiling with low inlet subcooling on the international space station, Int. J. Heat Mass Transfer 217 (2023) 124644, https://doi.org/10.1016/j.ijheatmasstransfer.2023.124644.